Study of Porosity in Uncoated Cemented Carbide Tools During Titanium Alloy Machining.

Cornelis Botermans
2023

LUNDS UNIVERSITET

Master Thesis in Production and Materials Engineering - MMTM01
CODEN:LUTMDN/(TMMV-5356)/1-49/2023
Division of Production and Materials Engineering
Lund University

Supvervisor: Rebecka Lindvall, PhD student
Industrial Supervisor: Susanne Norgren, Adjunct Professor
Examiner: Filip Lenrick, Lector

Author: Cornelis Botermans
Lund, Sweden, 2023

Avdelningen för Industriell Produktion
Lunds Tekniska Högskola
Lunds Universitet
Box 118
221 00 Lund
Sverige

Division of Production and Materials Engineering
LTH, School of Engineering
Lund University
Box 118
SE-221 00 Lund
Sweden

Printed in Sweden
Media-Tryck
Lund University

Abstract

During high speed machining of titanium alloys both the tool and workpiece material diffuse into one another affecting the surface integrity of the cutting tool edge and leading to fracture. One proposed mechanism by which the tool integrity is compromised results from the possible formation of porosity in to subsurface of the tool substrate close to the tool cutting edge. In this study the porosity in uncoated cemented carbide tools during titanium alloy machining is investigated. In order to simulate the diffusion process, diffusion couples between titanium and WC-6%Co are studied at various pressure (0 - 2.5 GPa) and temperature (800-1200 °C) conditions. Cross sectioned diffusion couples were analysed with SEM and XEDS. Pore formation was identified in two of the 6 samples that were analysed. The cause is unknown but believed to be Kirkendall porosity, where vacancies nucleate due to a net flux of vacancies towards the insert. As part of this study worn milling and turning inserts were also investigated. No voids were observed during analysis of the cross sectioned turning insert. In one milling insert groups of cavities are found in the binder phase, however, these are believed to not be formed by diffusion wear, but rather by plastic deformation. The presence of voids along the cutting edge is observed in one insert, the origin of these cavities are unknown. It's the first time that porosity in titanium machining has been the focus of a study and it progresses the field forward.

Acknowledgements

This master thesis was performed at the Division of Production and Materials Engineering at the department of Mechanical Engineering Sciences at LTH. The project is in close collaboration with Sandvik Coromant. This master thesis is the final work for the Engineering Nanoscience Programme and is accomplished in the spring and summer of 2023.

I would like to thank Mikael Hörndahl at the Division of Production and Materials Engineering for machining the titanium samples and Filip Lenrick for being the examiner. At Sandvik Coromant I want to thank Krister Edlund for annealing the samples, Christer Fahlgren for the sample preparation, Lars Gustafsson for providing worn milling inserts and Changhong Xiao for guiding me during the SEM imaging.

Many thanks to my supervisors Rebecka Lindvall, Susanne Norgren and Alex Graves for the fortnightly meetings. Thank you for sharing your knowledge, being constructive, encouraging and guiding me throughout the project. Special thanks to Rebecka, you were always available and offered your time during the SEM imaging and sample preparation sessions.

Finally, I would like to thank family and friends.

Contents

1 Introduction

Titanium alloys have a high tensile strength, corrosion resistance, toughness and are light weight relative to other metals used in similar applications. The drawback is the high cost of material and processing which limits the applications to performance components in industries such as aviation [1] [2]. Cemented carbide tools are used when machining titanium due to its strength and hardness, the most common cemented carbide consists of WC grains with a Co metal binder. A leading company that manufactures cemented carbide cutting tools is Sandvik Coromant. They produce an extensive range of metalworking cutting tools for procedures such as milling, drilling and turning. Although cemented carbide is a hard material, the tools are affected by wear and degradation during machining [3]. Chemical and diffusion wear is significant during Ti machining, where interaction between the tool and workpiece material weakens the insert. These wear mechanisms are increased at elevated temperatures and are apparent during titanium machining due to the low thermal conductivity of titanium [4]. Diffusion couple investigation between cemented carbide and titanium has been conducted to elucidate the diffusion, the technique partly mimics the machining process at high temperature and various pressure. Graves et al. [5] has examined a diffusion couple and found characteristic pores in the cemented carbide. With the help of simulations the calculated permeability of Co in Ti-Al(5%)-V(5%) is high. Therefore it is believed that the pores found in the diffusion couple might be Kirkendall pores. These voids are formed when there is a difference in permeability between two materials.

This thesis investigates the origin of these pores and if they are found in other diffusion couples, throughout this report voids, pores and cavities will be used interchangeably. In the second part of this project worn inserts are investigated, where the aim is to conclude if cavities are formed in the inserts during machining. If pores are found, it is of significance since it implies that the cutting edge is weakened and the pores formed from the inside could enhance cutting edge breakage. The pores weaken the mechanical integrity of the tool and thus decreases the wear resistance. This study will also compare the results to the current state of the art in the field. The investigation will contribute to further understanding of diffusion wear and possible porosity creation during titanium machining. This study will also take a systematic approach with a range of pressure and temperature to conclude where at the cutting edge pores are formed. Different testing methods like turning and milling operations, diffusion couples are used with two commercial Ti-alloys. The study aims to investigate if, where and when pores are formed during titanium machining, in order to design new tool material.

2 Theory

2.1 Titanium and its alloys

Titanium is twice as heavy as aluminum but half the weight of nickel and iron. The interesting properties of titanium is its high specific strength and corrosion resistance [6]. The thermal conductivity of titanium is poor which is an issue during the machining process since excess heat is difficult to remove [7].

Titanium is crystallized into various crystal structures within specific temperature ranges. At low temperature pure titanium forms a hexagonal close packed structure (hcp) which is called α-titanium [1]. At high temperatures the body-centered cubic (bcc) structure is stable and is called β-titanium. The β-transus temperature is 882 °C. The alloying elements of titanium are classified according to their effect on the β-transus temperature, the classes are β-stabilizers, α-stabilizers and neutral see figure 1. The β-stabilizers lowers the β-phase while α-stabilizers elevate the α-phase to higher temperatures, neutral stabilizers have little effect on the β-transus temperature. The β-stabilizers are divided into β-isomorphous and β-eutectoid, β-isomorphous elements are important due to their high solubility in titanium. β-eutectoid elements have a low solubility in titanium hence leading to formation of inter-metallic compounds. The alloying elements used as α-stabilizers are Al, O, N and C where Al is most common. β-isomorphous are e.g. Mo, V and Ta, β-eutectoid stabilizers are e.g. Co, Fe, Cr and Mn [1][8].

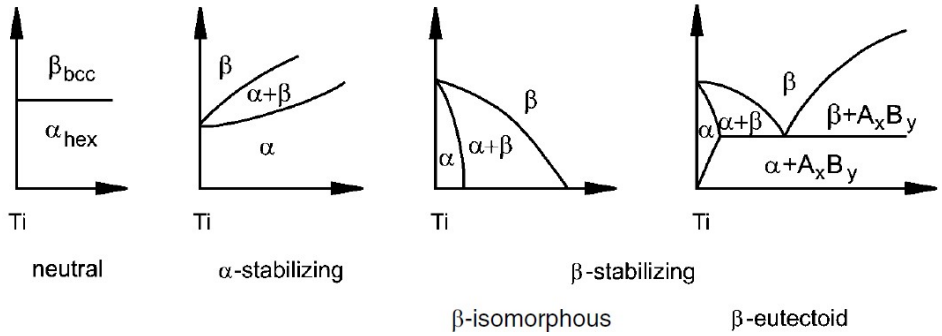

Figure 1: The effect element stabilizers has on the titanium phase diagram [6]. X-axis represents amount of stabilizing element and y-axis the temperature.

Titanium alloys are grouped into α, near α, α+ β, metastable β and β alloys. α alloys range from pure titanium to titanium alloys solely with neutral and α-stabilizing elements. Near α alloys are alloyed with small fractions of β-stabilizers. The $\alpha + \beta$ alloy group consists of both α and β in several different microstructures, at room temperature the volume fraction of β is restricted to 5-40 % [6]. When the level of β-stabilizers is increased to a level where the titanium no longer forms martensite, a lamellar $\alpha + \beta$ microstructure, the alloys are included in the metastable β group. The last alloy group consists of the single β phase.

The $\alpha + \beta$ alloy group is the most widely used, whereas Ti6Al4V is the most extensive and frequently used Ti-alloy, often referred to as Ti-64 [6]. The most recognized metastable β -alloy is Ti5Al5V5Mo3Cr, known as Ti-5553.

2.2 Cemented carbide

A considerable proportion of cutting tools consists of cemented carbide. The constituents of cemented carbide are irregular carbide grains embedded in a binder metal. The carbides are hard and brittle whereas the binder is ductile and provide a solid specimen without cavities between the carbide grains. The carbides provide wear resistance and contain mainly tungsten carbide (WC) but other carbides can be present such as titanium, tantalum, zirconium and hafnium carbides [3]. The binder is in most cases cobalt, however

iron and nickel alloys can also be present. The inserts are manufactured by combining the binder metal and carbide grains in powder form, thereafter mold into shape and afterward sintered. Cobalt has two allotropic structures, a closed-packed hexagonal (hcp) form, stable at temperatures below 400 °C and face centered cubic form (fcc). In cobalt powder a mixture of the two lattice structures are present. Sintered cobalt in the cemented carbide has mainly a cubic lattice, it is not transformed to hcp form after the annealing process. This is due to mechanical constraints between the WC matrix and dissolved W and C that stabilize the cubic modification [9]. The transformation temperature from hcp to fcc is mainly dependent on the W content where an increase of dissolved W raises the transformation temperature [10]. Depending on the sought properties required of the cemented carbide, the fraction of cobalt and WC grain size are adjusted to get the desired toughness and hardness. Cemented carbide is generally used as the material in cutting tool inserts in machining due to their high hardness, most types of cemented carbide inserts are coated to enhance the hardness and grant chemical resistance. During titanium machining, the predominant cutting tool material is uncoated WC-Co.

2.3 Machining

Machining is a process in which workpiece material is removed through cutting material with a cutting tool/insert. A relative motion between the workpiece and the sharp insert shears workpiece chip material from the workpiece. The insert has two sides which are in contact with the workpiece, the chip travels along the rake face and the flank face against the newly machined workpiece as shown in figure 2c. Several different machining operations are available, most common milling, turning and drilling, in this study milling and turning is used.

2.3.1 Turning

In a turning process, the work material is held in place using a lathe chuck and rotated. The tool is held against the workpiece using a mobile tool holder, the tool is fed against the workpiece and moved parallel to the workpiece surface removing material. Turning generates cylindrical workpiece components since the definition is that the workpiece is rotating. Depending on the tool different types of applications are manageable such as longitudinal or profiling, internal or external turning. Longitudinal external turning is used in the following study where the tool is continuously engaged with the work material, but the tool can also engage periodically [11]. Some material require cutting fluid during machining in order to cool the machining area, flushing chips away and through lubrication thus reducing friction.

During machining, operating parameters are set by the operator such as the cutting speed (v_c) which is the speed the tool travels along the workpiece [m/min] [12]. The cutting speed is determined by the rotational speed of the spindle and the workpiece diameter. The feed (f) is the axial advancement of the tool per workpiece revolution [mm/rev]. The depth of the cut (a_p) is the thickness of the material that is removed at each pass, the turning parameters are presented in figure 2a.

2.3.2 Milling

In a milling process, the workpiece is fixed while the material is removed by a rotating cutter where the rotating cutter often has several tool teeth which vary between one to several hundred teeth. Either the clamped workpiece, rotating toolpiece or both moves during machining to generate the desired component [13]. Milling can be categorised into peripheral milling and face milling, peripheral milling generates a surface plane parallel to the rotation axis. Face milling creates a surface normal to the axis of rotation and is used for wide plane workpieces. During milling operation the insert engage intermittently since each tool is cutting only during less than half of a revolution. The relation between the rotating toolpiece and workpiece is divided into up and down-milling. In up-milling the cutting tool rotates in the same direction as the feed direction therefore creating a chip thickness which starts at zero and gradually increases until the tooth breaks contact with the work surface. In down-milling the cutter is rotating in opposite direction, where the

chip thickness is at maximum at initial tool contact and is gradually decreased to zero [11]. Like the turning process cooling fluid may be used during milling.

Throughout milling several parameters are of importance. The cutting speed (v_c) [m/min] of the tool, the feed per tooth (f_z) [mm] which is the linear movement parallel to the cutting speed for each tooth. The axial depth (a_p) [mm] of the material removed, radial depth of the cut (a_e) [mm] which is the distance perpendicular to the axis and the set cutter diameter (DC) [mm] see figure 2b.

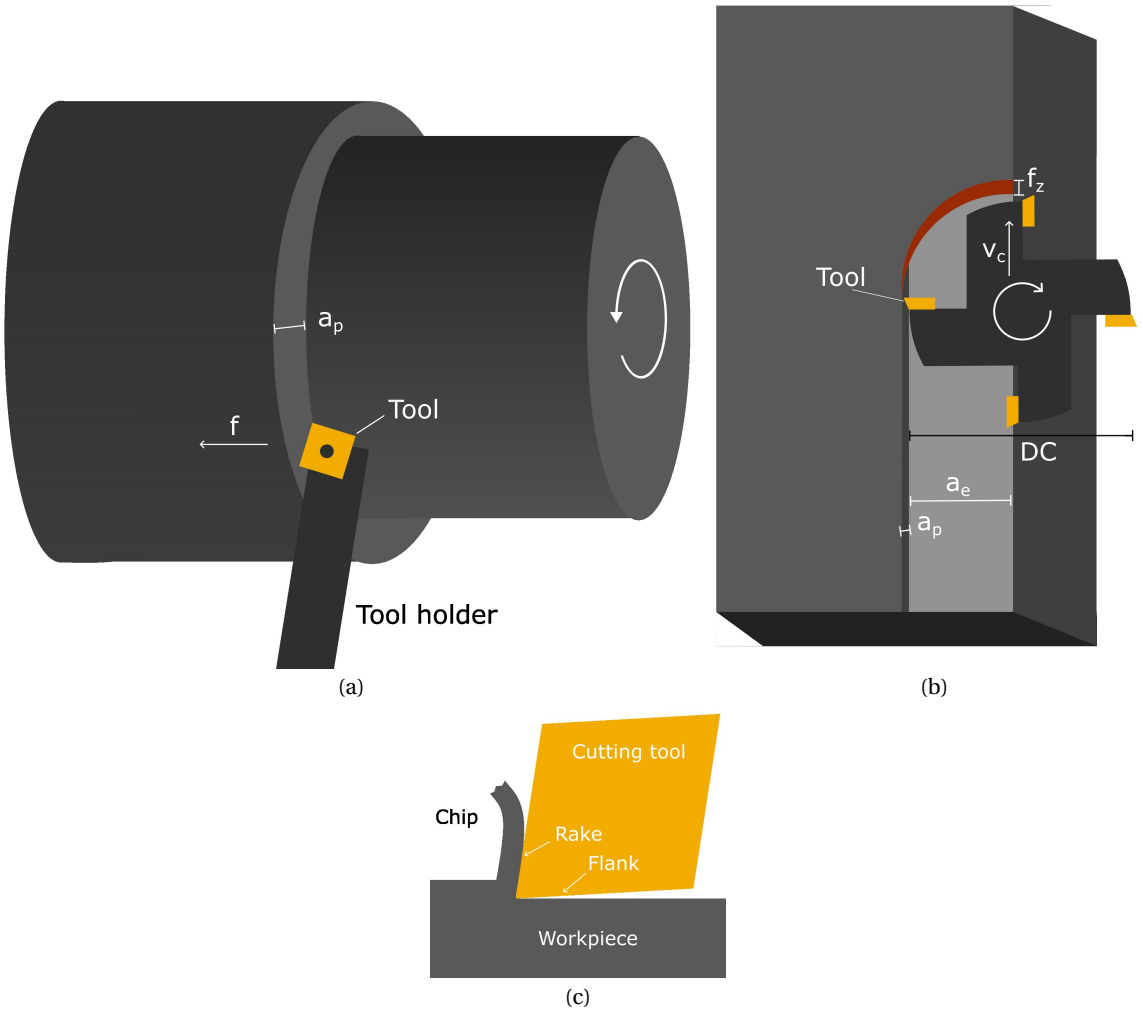

Figure 2: Schematic illustration of the a) turning and b) up-milling process with important machining parameters, c) cross-section of tool and workpiece.

2.4 Wear mechanisms

Wear mechanisms are the underlying mechanisms that manifest into certain wear types. Tool wear is classified according to the location and characteristics. The different types are notch, crater and flank wear, see figure 3a. Notch wear occurs at the depth of cut line where the tool pushes against the shoulder of the workpiece, notch wear forms at both the rake and flank face of the tool. The notch wear leads to burr formation on the workpiece and in severe cases failure of the cutting tool. Crater wear forms on the rake face where the chip slides along the chip-tool interface in the chip flow direction (CFD) [14]. Flank wear occurs between

the flank face of the tool and the machined workpiece. In order to evaluate the dimensional accuracy during machining both the width of the flank wear and depth of the crater wear is used as tool wear criteria [13].

During machining the friction leads to high temperature at the cutting edge. Using the simulation program Advantedge Odelros et al. [15] simulated the temperature at the cutting zone during titanium machining, at v_c 115 m/min and f 0.2 mm/rev the temperature at the rake face exceeds 1000 °C as shown in figure 3b. The pressure at the tool/chip interface can reach pressure up to 2 GPa. The pressure is calculated on the rake face where it varies from the highest pressure 2 GPa to no pressure at where the chip leaves contact with the insert [15].

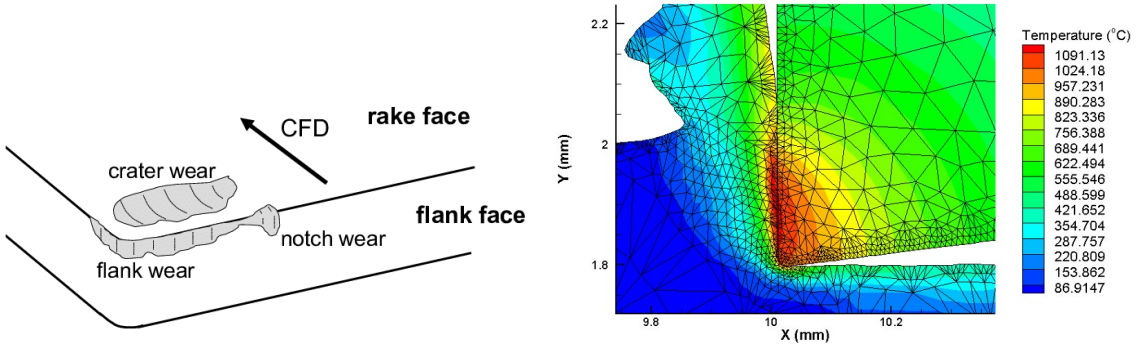

(a) (b)

Figure 3: a) Schematic figure highlighting the crater, flank and notch wear [14]. b) Temperature distribution simulation of the cutting zone during titanium machining at v_c 115 m/min and f 0.2 mm/rev [15].

2.4.1 Mechanical wear

Mechanical wear is characterised buy tool wear that is caused by mechanical damage. Tool fracture is a larger scale breakage and occurs suddenly due to substantial stress fluctuations in the cutting force. The brittleness of the cemented carbide renders severe cracking by the load gradient and often occurs during milling where the insert is continuously interrupted. Fracture leads to breakage of the tool. Chipping is a diminutive fracture wear which occurs at the cutting edge at dimensions 5-50 µm. Similar to fracture chipping happens instantaneously when cutting force changes suddenly for example in a workpiece that has hardness irregularities [16].

Abrasive wear involves the removal of toolpiece material caused by sliding hard particles against the cutting tool. Hard phases such as inclusions in the workpiece or particles broken away from the cutting tool erode the cemented carbide. Abrasive wear is affected by the relation between the hardness of the tool and the workpiece material. Abrasive wear is moderately affected by cutting temperature, when the cutting temperature increases the cutting tool hardness decreases which leads to more abrasive wear [17].

2.4.2 Plastic deformation wear

The plastic deformation wear type is observed at high temperatures when the insert is unable to withstand the compressive stress. The cutting edge deforms resulting in improper insert shape decreasing the machinability, the blunt edge cause additional heat source leading to plastic collapse of the material. Plastic deformation is influenced by the thermomechanical load on the tool during cut, therefore, the amount of plastic deformation increases with higher cutting temperatures at high feed rate [17].

For WC-Co cemented carbides at low temperature the deformation is elastically but at temperatures higher than 800 °C plastic deformation is more prevalent. Plastic deformation is believed to occur both through dislocation movement and grain boundary sliding [18]. Together with grain boundary sliding the binder phase permeate the WC/WC boundaries forming lamellae phase which has been observed in both worn turning

inserts and hot compression tests [19][20]. Intergranular cavities in the Co binder phase are observed in the binder phase during hot compression creep testing [20]. In worn turning inserts similar cavities and cracks along the binder phase are formed, the cavities are not spherical but of irregular shape and a result of plastic deformation wear [18].

2.4.3 Adhesive wear

Adhesive wear occurs when work or chip material welds to the tool which requires high temperature and pressure. The adhered material to the cutting tool forms a built up edge (BUE). When the BUE is removed due to high shear stress tool particles adhered to the BUE fractures from the cutting edge, the adhesive junction results in brittle carbide particles being sheared off within the tool. Adhesive wear occurs when workpiece material repeatedly adheres and breaks away from the tool material resulting in damage to the tool. At low temperatures, adhesive wear is minimal due to low adhesion tendency similarly at high temperatures the BUE rupture is moved from within the tool back to the adhered layer interface because of thermal softening. Therefore the adhesive wear is most severe at intermediate temperatures [17].

2.4.4 Diffusion wear and chemical wear

Diffusion wear involves mutual diffusion between the cemented carbide and workpiece material. Diffusion wear is enhanced by elevated temperature due to higher diffusion rates. The diffusion wear process cause deterioration of the tool material weakening the cutting tool, consequently both the adhesive and abrasive wear increases [17].

Chemical wear occurs when new chemical compounds are formed between the air, cutting fluid, work or tool material. For example when oxygen in the air reacts with the cutting tool and workpiece material, known as oxidation wear. Both chemical and diffusion wear can be opposed by coating the cutting tools [17].

2.4.5 Wear in Titanium machining

Tool wear in titanium machining is an aggregate of abrasion, plastic deformation, chemical/diffusion and adhesion wear. In titanium machining mechanical wear dominates at low cutting speeds, whereas plastic deformation and diffusion wear are superior at higher cutting speeds. The tool life in Ti-machining is primarily govern by crater wear [21]. Crater wear is the superior wear type which grows at a consistent rate. The crater wear changes the cutting geometry which leads to plastic deformation, chipping and fracture. Due to the low thermal conductivity of Ti-alloys, the cutting zone reaches high temperatures even at low machining speed. The high cutting temperatures are due to low heat dissipation through the Ti-chip. Cutting temperature are estimated to be well above 1000 °C at the cutting surface depending on the cutting speed and feed rate [22]. Simulations using FEM confirm the high temperature above 1000 °C during Ti-machining [15]. The high temperature at the tool chip interface advance and accelerate the diffusion wear.

Both workpiece material and toolpiece material diffuse into one another traces of Ti, AL and V are found in worn inserts when machining Ti-64 [23]. The cemented carbide constituents diffuse into the titanium, this occurs both at the rake and flank during milling and turning [24]. Due to the continuous chip renewal the saturation of tool material in the workpiece material is not enabled. Carbon depletion of the WC grains due to outwards diffusion leads to bcc-W formation [25]. The chemical reaction between Ti and C forms adherent TiC which is found in small quantities between the tool and Ti during turning [26][27][25]. It is suggested that the TiC are continuously removed during machining. Simultaneous C from the WC grains diffuse to the interface creating new TiC. The TiC grains are diffusion wear limiting the cutting tools constituents outwards to the chip, retarding the diffusion wear.

Due to the dynamic nature of machining the diffusion and chemical wear is difficult to investigate, therefore diffusion couples have been studied where the resulting chemical product and diffusion is not removed. In the diffusion couples a (Ti,V)C band layer is seen between Ti-64 and cemented carbide diffusion couples, Ti

diffusion into the cemented carbide is also observed. The depletion of carbon in the WC grains leads to formation of bcc-W, although W diffusion into the Ti is measured. Below the TiC layer a η-phase (M_6C/W_3Co_3C or $M_{12}C/W_6Co_6C$) is observed in the binder phase, the η-phase is brittle which forms quickly during mechanical load [28]. The formation of the η-phase is believed to form due to outwards Co diffusion to the Ti and concurrently W and C diffusion from the WC grain to the binder phase [29][30][25]. Pores and cavities are seen in the η-phase of a cemented carbide/Ti-5553 diffusion couple, it is proposed that this might be due to Kirkendall effect where Co diffusion outwards is not complemented by workpiece material inwards resulting in cavities [5]. The η-phase observed in the static diffusion couples has not been detected in machining which indicates a discrepancy in the diffusion couple experiment. Another discrepancy with the diffusion couple studies is the static work material which during machining is continuously renewed such that no saturation of the diffusing elements is reached in the Ti.

2.5 Kirkendall effect

In 1929 Pfeil et al. [31] discovered that small impurity particles on oxidising iron were gradually buried by iron oxide and eventually covered. The particles act as inert material and do not take part in the reaction between iron and oxygen. The resulting iron oxide grows at the oxide/air interface which indicates that Fe diffuses faster through the oxide compared to O_2. In 1947 Smigelkas and Kirkendall [32] reported the inequality of the diffusivities in the Cu-Zn binary system, they used molybdenum wires as inert markers. In the experiment, a wrought brass (70 wt% Cu-30 wt% Zn) bar is used and along the surface Mo wires are placed. The Mo wires function as markers during the diffusion process, the plane at which the markers lay in is called the Kirkendall plane. The bar is thereafter coated with a copper layer. The sample is annealed at 785 °C at which the Cu and wrought brass diffuse into one another, at different time intervals the diffusion couple is cross sectioned. The result showed that with increasing annealing time the thickness of the resulting α-brass (Cu_3Zn) product grew. During the diffusion process the molybdenum markers moved towards the center of the bar, see figure 4. From the experiment conclusions were made, the rate of diffusion of zinc in α-brass is greater than copper in α-brass and the unequal diffusion rates shift the Kirkendall plane. Prior to Kirkendalls experiment the diffusion mechanism was believed to be a ring mechanism in solid-state, where two neighbouring atoms swap place in a ring motion. The experiment is inexplicably with the ring mechanism diffusion since the diffusivities would be the same. A vacancy diffusion mechanism was proposed where atoms move from their origin site to a neighboring vacant lattice site. This results in a vacancy flow in the opposite direction of the faster diffusing Zn.

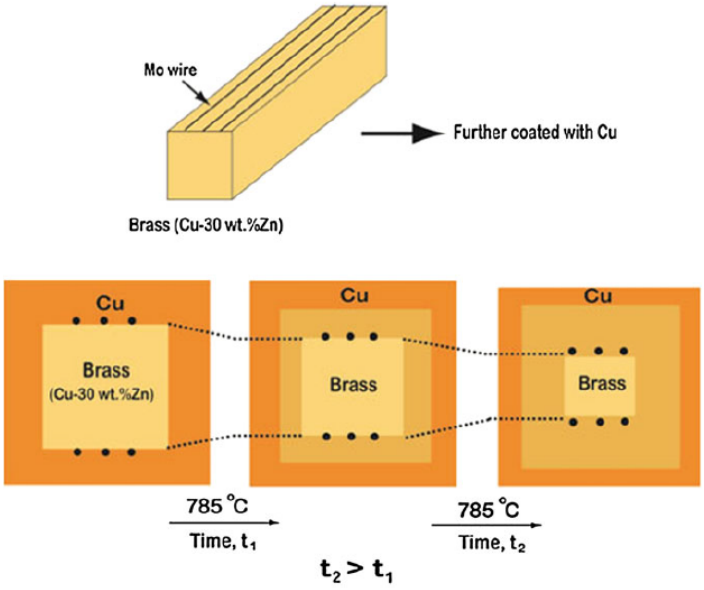

Figure 4: Schematic illustration of Kirkendalls experiment [32], figure adapted with permission from [33].

From Kirkendall's experiment the diffusion process would henceforward be explained in consideration of all components flux and diffusion coefficients. A binary diffusion couple of component A and B with inert markers applied at the A/B interface, the initial plane at the markers is denoted x_0 and more specific the Matano plane x_M when the volume change during the diffusion couple is zero. During annealing component A diffuses into component B and vice versa, the diffusivities of the different species is denoted D_i which is called the intrinsic diffusion coefficient, where i is the element [34]. The diffusion of both elements generate a diffusion zone where either a new phase forms based on component A and B or a concentration profile curve in the shape of an error function.

Assuming that no phase is formed between component A and B and that their intrinsic diffusivity is equal the flux are also equal ($|F_A|=|F_B|$) in the diffusion zone. The result will be a motionless marker plane, since an equal quantity of component A and B intersect the initial junction as seen in figure 5a. Suppose that diffusion only occur by vacancy mechanism and the intrinsic diffusivities are unequal where element B diffuses faster, the resulting diffusion flux difference ($|F_A|<|F_B|$) leads to a net flow of atoms past the inert markers from side B to A. This shift causes the diffusion couple to move with respect to the markers in the direction with the net element flux. From the perspective of the Matano plane the inert markers move in opposite direction from the net flux. The movement of the inert markers follows the Kirkendall plane (x_k) which is defined as the marker plane which stays at a constant composition during the annealing process [35]. The rate at which the kirkendall plane moves is $v_K=x_K/2t$, where v_K is the velocity and t the annealing time. A net flow of atoms moves towards the A side which implies a vacancy diffusion towards side B due to diffusion occurring via vacancy mechanism, see figure 5b. The vacancies are created at the A side and absorbed at the B side. The vacancies are generated at sources and eliminated at sinks at either grain boundaries, pores, cracks or dislocations. Edge dislocations arise where the lattice has an additional half-plane, on the B side these act as sinks where the vacancies displace the atoms along the edge dislocation. Identical the edge dislocation acts as sources on the A side where vacancies are created due to growing edge dislocations, atoms are added to the extra plane, therefore, vacancies are created and move to neighbor positions [36].

In many diffusion couples where the Kirkendall effect is observed one interesting feature is noticed, pores are found in the diffusion couple on the side towards where the Kirkendall plane moves. The reason for this feature is the lack of sinks, the vacancies coalesce to form voids. The volume of these pores affects the

Kirkendall plane shift, in the presence of cavities the marker plane movement is less. The Kirkendall shift and Kirkendall pores are two competitive phenomena, in figure 5c voids are formed which oppress the Kirkendall plane shift. Kirkendall pores are moreover believed to form in diffusion couples with insufficient plastic relaxation [37]. In diffusion systems where the diffusion rate between element A and B is considerable, Kirkendall porosity is more likely. Besides the formation of voids, the diffusion couple develop internal stress. On the side where extra atoms are accommodated compressive stress evolves due to swelling. On the other side where vacancies accumulate, it shrinks and tensile stress develops [33].

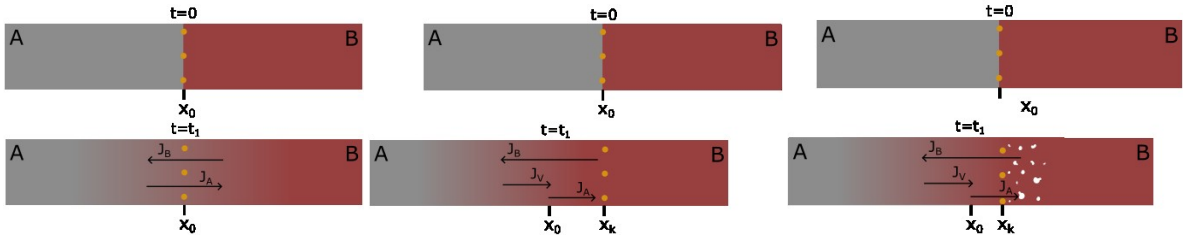

Figure 5: Schemateic illustration of the Kirkenall effect, the flux is as following a) $|F_A|=|F_B|$ b and c) $|F_A|<|F_B|$. Kirkendall porosity is formed in figure c where the vacancies coalesce.

2.5.1 Kirkendall porosity examples

Paul et al. [38] conducted a diffusion couple experiment between Nb and a mixture of Nb_5Si_3 + $NbSi_2$ (Nb-57 at.% Si). The temperature was 1325 °C for 24 h in vacuum. Between the diffusion couples particles of TiO_2 were used as Kirkendall markers. As seen in figure 6 the diffusion couple has two distinct phases in the diffusion zone, at one side of the Kirkendall plane (K) Nb_5Si_3 is formed. On the opposite side of the Kirkendall plane porous Nb_5Si_3 is formed. The presence of these Kirkendall pores and the movement of the Kirkendall plane indicates that the diffusion rate of Si is much higher in the interdiffusion zone compared to Nb. The difference in diffusivities causes a vacancy flux in the opposite direction to the movement of Si. The calculated ratio between the Si and Nb intrinsic diffusion coefficient is $\frac{D^*_{Si}}{D^*_{Nb}} = 31 \pm 15$.

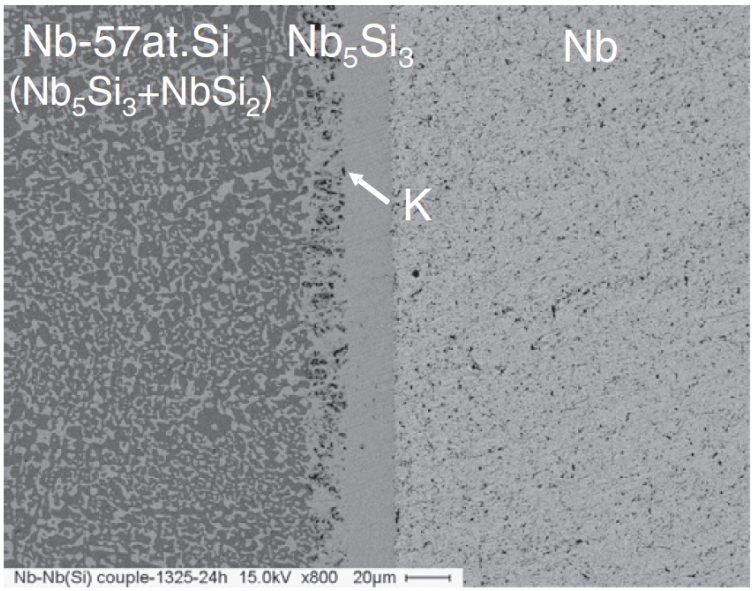

Figure 6: Cross-section SEM image of Nb-57at%Si/Nb diffusion couple annealed at 1325 °C for 24 hours, Kirkendall porosity is observed in the Nb_5Si_3 product layer [38].

In the Ni-Cu laminate diffusion couples, the Cu diffuses faster into Ni compared to Ni into Cu. The net flow of vacancies results in Kirkendall porosity in the Cu layers [39]. The Ni-Cu diffusion couple is annealed in a vacuum at 1000 °C for 1, 10 min and 24 hours, see figure 7. The voids found in the samples are of irregular size and increased in size with increasing annealing resulting in coalescence of multiple pores.

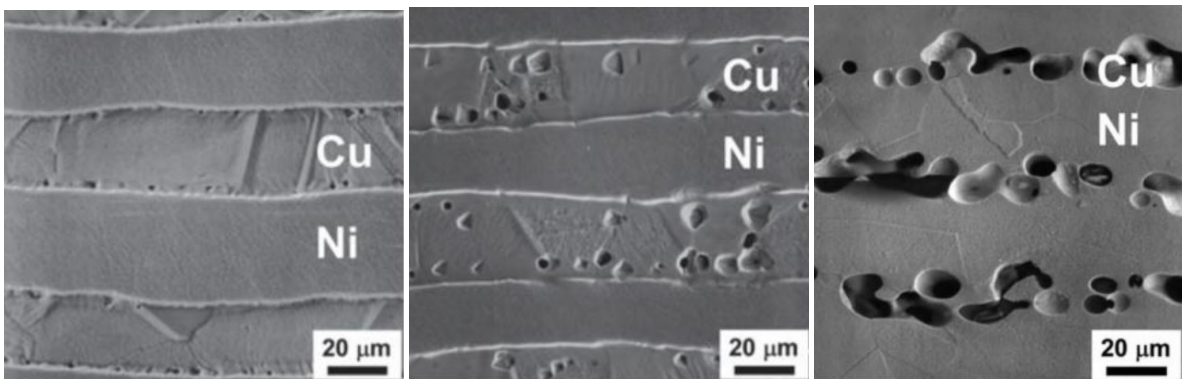

(a) (b) (c)

Figure 7: Cross-section SEM image of Cu/Ni diffusion couple annealed at 1000 °C for a) 1 min, b) 10 min and c) 24 hours, Kirkendall porosity is observed in the Cu layer [39]

2.5.2 Cobalt diffusion in Titanium

The first diffusion coefficient of Co in polycrystal α-Ti was measured by Santos et al. [40] at 799° and 856°C. A more extensive measurement of the diffusion of Co in single crystal α-Ti was conducted by Nakajima et al.[41]. The diffusion anisotropy is studied in parallel $D_{\parallel}$ and perpendicular $D_{\perp}$ to the c axis of the α-Ti hcp crystal structure. The relation between the anistropy diffusivities where $D_{\parallel} > D_{\perp}$, Santos measured diffusion coefficient is between $D_{\perp}$ and $D_{\parallel}$. At 862 °C the diffusivity is measured to $D_{\parallel} = 1.054 * 10^{-11}$ and

$D_\perp = 5.066 * 10^{-12}\ m^2/s$. Nakajima combined the crystallographic directions diffusivities to an average diffusion coefficient for α-Ti using the following equation: $D_\alpha = (2D_\perp + D_\parallel)/3$. The high Co diffusivity in α-Ti is about five orders of magnitude faster than the self-diffusivity in α-Ti measured by Dyment et al. [42]. It is generally accepted that the vacancy mechanism is in force for self-diffusion of Ti, therefore impurity atoms that diffuse with substitutional diffusion are expected to have similar magnitudes of diffusion. Since Co diffuses five orders of magnitude higher than the self-diffusivity in α-Ti it is believed that Co diffuses with an interstitial mechanism. Nakajima submits another reason for possible interstitial diffusion of Co, if vacancy diffusion is operative for Co diffusion the self-diffusion should increase. Unfortunately, there are no studies on the Co affect on the self-diffusion in α-Ti, although Dyment has studied the self-diffusion in β-Ti [43]. Dyment concluded that Co addition to Ti is less than the theoretical minimum value expected for vacancy mechanism. From this Nakajima considers it unlikely that Co atoms diffuse with a vacancy mechanism. Compared to Co diffusion in α-Ti the diffusion in β-Ti is lower at the α/βtransition [44]. The diffusion coefficient for Co in α-Ti and β-Ti is shown in figure 8, where the diffusion follows Arrhenius relationship $D = D_0 e^{-Q/RT}$. Q is the activation energy, D_0 is the pre-exponentional factor, R the gas constant and T the temperature [45].

2.5.3 Titanium diffusion in Cobalt

Neumeier et al. [46] investigated the diffusivity of Ti in fcc Co by binary diffusion couples at 1100-1300 °C. The diffusion couple consists of Co/Co-6at%Ti, the samples were annealed for 200, 150 and 75 hours and thereafter a composition map was measured perpendicular to the diffusion couple. From the resulting s-shaped concentration curve the activation energy and pre-exponentional factor are obtained, the diffusion coefficient is shown in figure 8. When studying the diffusion couple Co/Ti, intermetallic phases form in the titanium-cobalt system, phases such as Co_3Ti, Co_2Ti, CoTi and $CoTi_2$ [47]. This is the reason for a small fraction of Ti in the Co/Co-6at%Ti diffusion couple when studying the Ti diffusion in Co, since no intermetallic phases would form during the annealing process.

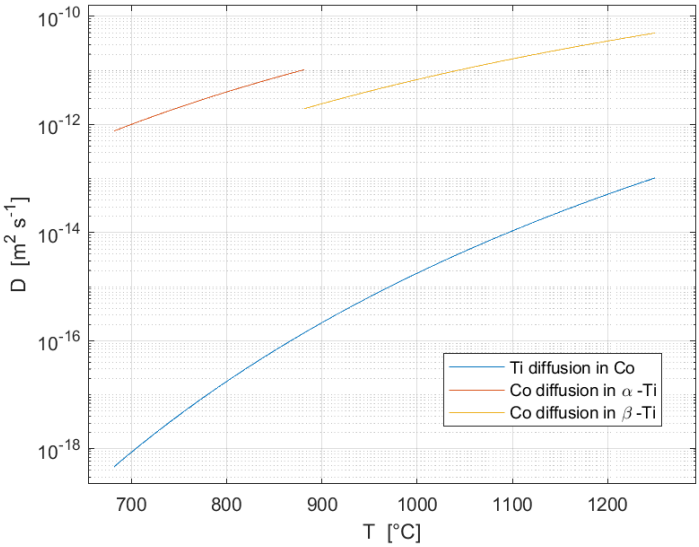

Figure 8: The diffusion coefficient for Ti in Co and Co in α and β-Ti.

2.5.4 Effect of pressure upon void formation

In 1957 Barnes et al. [48] experimented with void formation at various pressures, the diffusion couple used was hot pressed copper/nickel sandwiches. Their result showed that a hydrostatic pressure of 9 MPa prevented void formation. They also annealed samples in vacuum to promote void formation, thereafter they

annealed the samples at various pressures. The result showed that a pressure above 16 MPa eliminates the voids already formed. During the collapse of the voids the shape is retained which indicates that the voids disintegrate by diffusion rather than a deformation process. In 1981 Klein et al. [49] further investigated the suppression of Kirkendall porosity with pressure, the material used was Nb-Cu wires coated with Sn. By annealing at different hydrostatic pressures the niobium is diffusesinto the Sn layer forming Nb_3Sn. At a pressure of 14 MPa the formation of Kirkendall voids is suppressed. Another sample that is pre-annealed in vacuum would contain considerable porosity, it is further annealed at a pressure of 16 MPa. After the heat treatment most pre-existing voids are eliminated. These experiments show that hydrostatic pressure both suppresses and eliminates Kirkendall porosity.

2.6 Experimental methods

2.6.1 Electronic discharge machining

Electrical discharge machining (EDM) is a precision machining method used for electrically conductive materials. EDM uses an anode and an electrode which are not in physical contact, the workpiece material is the anode while the tool is the electrode [50]. Using a discharge of electrical pulses sparks are formed between the anode and electrode. The voltage between the anode and electrode creates a plasma which heats the workpiece and tool material to the point where it vaporizes. The process is submerged in a dielectric fluid which functions as cooling and an electrical insulator that switches to a conductor at high voltage. Wire-cut EDM uses a wire that continuously travels past the workpiece, the wire is controlled by computer numerical control (CNC) to produce complex workpiece geometries. A portion of the vaporized material ejected from the surface re-solidifies on the workpiece, this layer is called white layer and consists of microcracks and high tensile residual stress [51]. Due to the high machining precision the process is used for sectioning titanium samples in this study.

2.6.2 Scanning electron microscopy

Scanning electron microscopy (SEM) is a method where a beam of electrons are sent at a sample from an electron source [52]. Most commonly a field emission gun (FEG) is used as the electron source and thereafter the electrons are accelerated to high energies in an electromagnetic field until the electrons extend energies between 2-30 keV. Electromagnetic lenses are used to focus and scan the electron beam along the sample and image stepwise the pixels. The electrons interact with the sample mainly in two ways, elastically where the electron interacts with the electric field of the nucleus and scatter in either low or high-angle. The high-angle scattered electrons have identical energy as the incident electrons. The electrons are called back scattered electron (BSE) if the electron goes back through the sample in the incident direction. The second interaction is inelastic when beam electrons interact with the specimen electrons resulting in a transfer of energy and emission of the specimen electron, these electrons are called secondary electrons (SE) and are by definition <50 eV. Due to the creation of SE, the vacancy formed has the possibility to be filled by a higher energy orbital electron, producing an X-ray. The energy of this X-ray is characteristic to the host element and is therefore useful during composition characterisation. The characteristic X-ray energies are measured with a detector and used in elemental analysis, energy-dispersive X-ray spectrscopy (XEDS). The elastic and inelastic specimen-beam interactions is distributed over a three-dimensional interaction volume. The interaction volume is specified as the escape depth from which the signal is not absorbed in the specimen, see figure 9. SE has a short escape depth of approximately 5-50 nm and is therefore surface characteristic, BSE has a greater escape volume while the characteristic X-rays has the biggest escape volume. The interaction volume translates to resolution, a larger interaction volume has a worse lateral resolution. The interaction volume is dependent on several parameters but most important the accelerating voltage and atomic number (Z) of the specimen, with lower accelerating voltage and higher atomic number the interaction volume is decreased. The measured BSE intensity is translated to the image contrast where higher intensity correlates to a higher brightness. Utilizing that the number of BSE in relation to the incident beam electrons are increased with increasing atomic number the main contrast in BSE images is density contrast (Z-contrast)[52]. The SE

is relatively insensitive to atomic number but rather the ridges and edges of the sample, many SE escape along edges which results in topographic contrast [52].

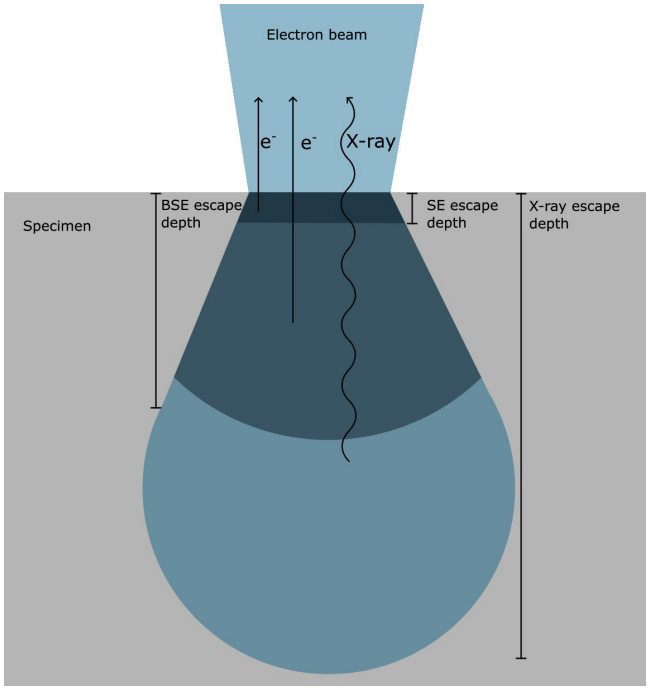

Figure 9: Schematic image of the escape depth of SE, BSE and characteristic X-rays.

3 Materials and Methods

Both Ti-64 and Ti-5553 diffusion couples are investigated. A part of this study also includes fabrication of diffusion couple samples, these samples are based on previous work [30]. Previous diffusion couple samples are furthermore studied, two samples 1200 °C Ti-64/cemented carbide 2.5 GPa and 1000 °C Ti-5553/H13A 35 MPa. The 2.5 GPa sample is part of a previous work [53] and the second 35 MPa diffusion couple is part of another work [5]. In the second part of this study cross sections of worn inserts are investigated. One turning insert of straight grade cemented carbide with 6% Co turned in Ti-64, this insert is previously studied [54]. Several worn milling inserts are also studied which were provided by Sandvik Coromant.

3.1 Diffusion couples

The diffusion couples are between the workpiece material Ti-5553 or Ti-64 together with cemented carbide tool H13A, H13A has a composition of WC-6wt%Co and WC grain size ~ 1μm. Microstructure of Ti-5553, Ti-64 and H13A are shown in figure 10. The composition of the workpiece materials is detailed in table 1. Three different methods are fabricated for the Ti-5553/H13A diffusion couples at various pressures, ~ 0 pressure, 35 MPa and 850 MPa. Similarly the Ti-64/H13A diffusion couples are fabricated at ~ 0 pressure, 850 MPa and 2.5 GPa depending on the experimental method. The ~ 0 pressure samples are assumed to be low pressure since the only pressure applied is the gravitational weight of the insert against the titanium. For the Ti-64/cemented carbide 2.5 GPa diffusion couple an insert with ISO RNGN060300 geometry is used. The remaining inserts are of CNMG 12 04 08-SM geometry and supplied by Sandvik Coromant.

Table 1: Compositional data of Ti-64 and Ti-5553, the major alloying elements and titanium is highlighted.

	Element wt%										
Sample	Mo	Zr	Fe	V	Al	C	O	N	Cr	Y	Ti
Ti-64	-	-	0.17	4.05	6.03	0.021	0.141	0.006	-	<0.005	Bal.
Ti-5553	4.58	<0.005	0.32	4.78	5.28	0.021	0.16	0.007	3.02	<0.001	Bal.

3.1.1 Ti-5553/H13A and Ti-64/H13A ~ 0 pressure

Ti-64 and Ti-5553 rods with 5.17 mm in diameter are fabricated using wire-EDM, the rods are grounded on two opposite sides with a file to create two parallel facets. An insert is divided into two pieces using Struers Secotom-50 with a diamond tip blade, a resulting 5 mm cemented carbide band is sectioned off. The cemented carbide and Ti diffusion couple is assembled as seen in figure 12a. The boarding diffusion surfaces are polished with 500 and 1200 silicon carbide grit paper. The diffusion couples are annealed in a FCT DEK50 sintering furnace under vacuum with a heating rate of 25 °C/min. The diffusion couples were treated for 120 min at temperatures 800, 1000 and 1200 °C, after the dwell time the samples were cooled with a cooling rate of 21 °C/min until 80 °C was reached which is presented in figure 11. Since the samples are pressurised during annealing and the insert and Ti is free to expand during heating no pressure is assumed at the diffusion interface. The samples are sectioned in half along the diffusion interface seen in figure 12a. The sectioned diffusion couple is further sample prepared, see section 3.3.

3.1.2 Ti-5553/H13A 35 MPa

The diffusion couple is created between the workpiece Ti-5553 and toolpiece H13A insert, 500 µm on the flank is polished away using a neoprene surface with diamond suspension. Thereafter the insert was placed in a graphite mould with a 20 mm internal diameter, 20 g of Ti-5553 powder with particle size 45-150 µm was added to surround the insert which during the sintering consolidated around the insert [5]. The diffusion couple is created with field assisted sintering technology (FAST) with a FCT Systeme HP D 25 SPS furnace. At the sintering process a constant pressure is held at 35 Mpa, the ramp rate was 100 °C/min and with a dwell time of 120 min at 1000 °C. The cooling rate was 100 °C/min from 1000 °C to 400 °C, the sintering program

is shown in figure 11. The sample is sectioned in half through the clamping hole, the sectioning is shown in figure 12c where the Ti is excluded. The sectioned diffusion couple is further sample prepared, see section 3.3.

3.1.3 Ti-5553/H13A and Ti-64/H13A 850 MPa

Ti-64 and Ti-5553 rods with 5.17 mm in diameter are fabricated using wire-EDM. The oxidised white layer on the rods are polished away with silicon carbide 1200 grid paper, the rods are polished until fitted in the insert clamping hole of 5.156 mm. The rods are cut to a length at slightly longer than the height of the insert 4.762 mm, the rods are deformed by mechanical compression using a vise in order to ensure good contact. The diffusion couples are annealed in a FCT DEK50 sintering furnace under vacuum pressure with a heating rate of 25 °C/min. The diffusion couples were treated for 120 min at temperatures 800, 1000 and 1200 °C, after the dwell time the samples were cooled with a cooling rate of 21 °C/min until 80 °C is reached which is presented in figure 11. During annealing the diffusion interface undergoes pressure due to higher thermal expansion of the Ti compared to the cemented carbide. The generated pressure is estimated to be 850 MPa for the Ti-64/H13A at 1000 °C, see appendix A. All samples are onwards named 850 MPa, even the Ti-5553, 800 and 1200 °C diffusion couple samples. The samples are sectioned in half along the diffusion interface seen in figure 12b. The sectioned diffusion couple is further prepared, see section 3.3.

3.1.4 Ti-64/cemented carbide 2.5 GPa

A fine grained WC with 6% Co circle tool is capsulated with a Ti-64 cylindrical capsule. The sample is annealed in high pressure with a HPAT–30 toroid-type high-pressure furnace [53]. During annealing, the diffusion couple is subjected to 2.5 GPa pressure, a ramp rate at 250 °C/min and a holding time of 1200 °C for 10 min. The sample was quenched in water and cross-sectioned using wire electrical discharge machining, the sample is sectioned parallel to the diameter of the round insert. The sectioned diffusion couple is further prepared, see section 3.3.

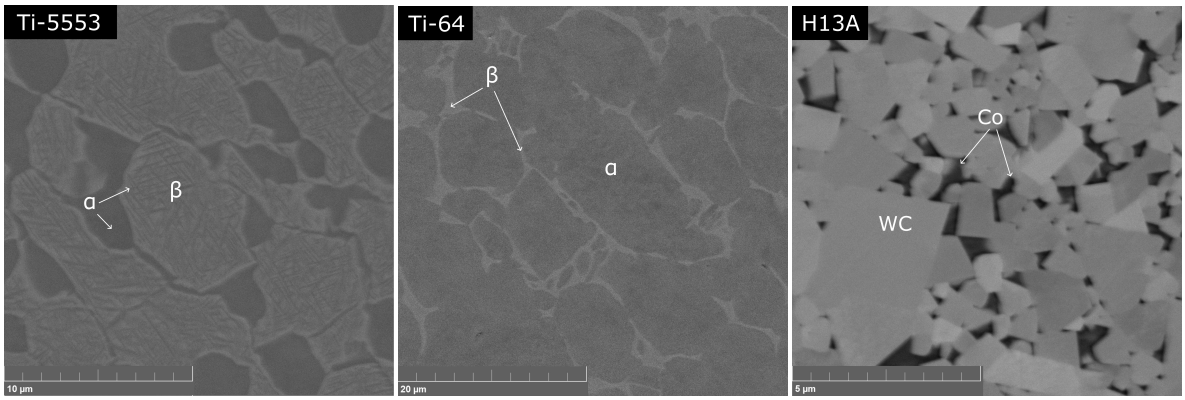

(a) (b) (c)

Figure 10: SEM images of the microstructure of (a) Ti-5553, (b) Ti-64 and (c) H13A. The α and β-Ti is highlighted in the titanium alloys, the H13A cemented carbide consist of WC grains and 6wt% Co binder.

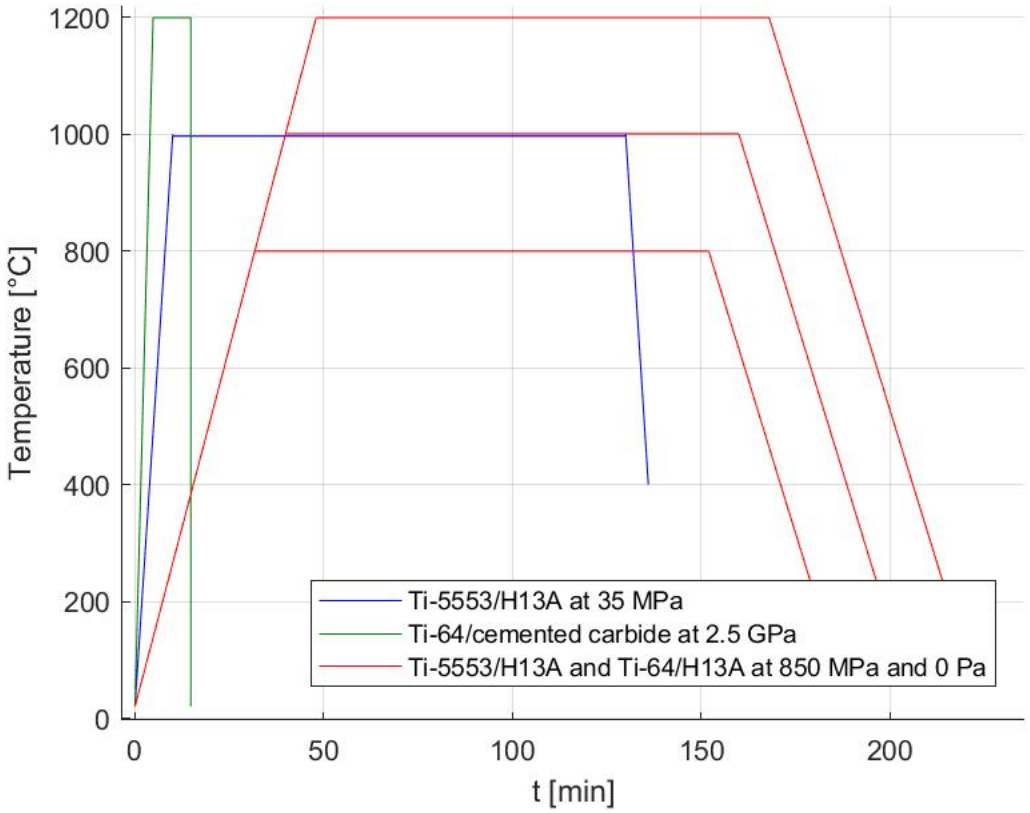

Figure 11: Sintering program for Ti-5553/H13A and Ti-64/H13A ~ 0 pressure, Ti-5553/H13A 35 MPa, Ti-5553/H13A and Ti-64/H13A 450 MPa and Ti-64/cemented carbide 2.5 GPa. Samples 0 and 450 MPa has various dwell temperatures at 800, 1000 or 1200 °C.

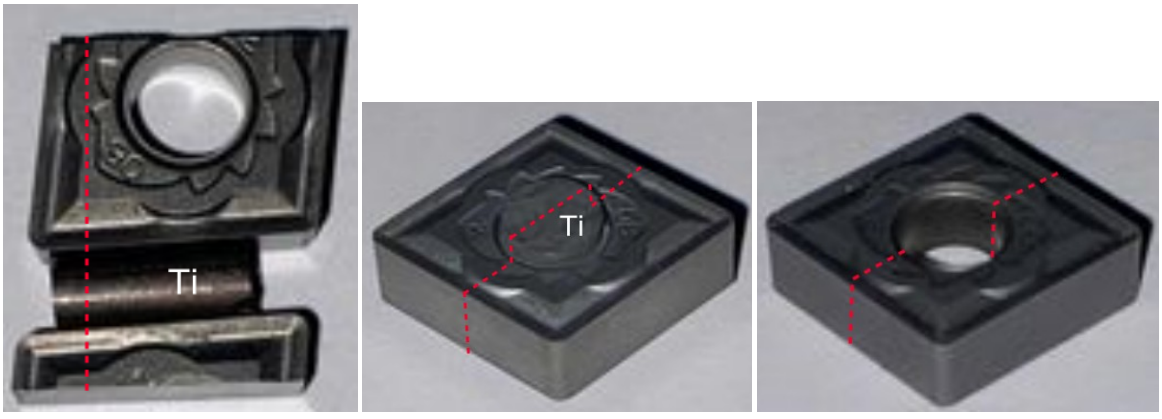

(a) (b) (c)

Figure 12: Diffusion couple image of a) Ti-5553/H13A and Ti-64/H13A ~ 0 pressure, b) Ti-5553/H13A and Ti-64/H13A 850 MPa and c) Ti-5553/H13A 35 MPa with the Ti-5553 excluded. The samples are cross-sectioned along the red striped line.

3.2 Worn tools

Both uncoated milling and turning inserts are used in machining in order to investigate worn tools. The insert geometry, Co and Cr content used in the study is presented in table 2. In total 5 milling inserts were investigated although only three inserts will be shown in this report, all milling inserts are provided by Sandvik Coromant. The turning insert is a fine grained WC-6%Co and studied previously in [54]. Both the milling and turning are machined with Ti-64 as workpiece material. The cutting data for each tool is seen in table 3. The turning was performed with the tool mounted in a SDJCL3225P11JET tool holder, the machine used is a CNC lathe SMT Sajo 500 Swedturn and cooling is applied on the rake [54]. The milling was conducted at Sandvik Coromant in Västberga.

Table 2: The samples geometry and composition content.

Sample	Process	Geometry	Co [wt%]	Cr [wt%]	WC [wt%]
T1	Turning	DCMT11T304-F1	6	unknown	Bal.
M1	Milling	R390-11T308M-MM	10.5	1.35	Bal.
M2	Milling	R390-11T308M-MM	13.5	0.52	Bal.
M3	Milling	R390-11T308M-MM	10	0.4	Bal.

Table 3: Cutting data for the cutting tools

Sample	v_c [m/min]	f_z [mm]	a_p [mm]	a_e [mm]	D_c [mm]	f [mm/rev]	Internal coolant [bar]	Time [min]
T1	200	-	0.3	-	-	0.10	90	4
M1	45	0.14	2	10	32	-	10	82
M2	45	0.14	2	10	32	-	10	28
M3	45	0.14	2	10	32	-	10	86

The machined inserts are ground perpendicular to the worn areas illustrated in figure 13 using Struers Accutom-100 precision cutting machine with a diamond cup wheel. Water mixed with Struers Corrozip fluid is sprayed continuously on the grinding blade in order to regulate the temperature. Material is gradually ground away with 100-250 µm intervals, in between each grinding instant a light optical microscope is used to assess if a satisfactory cross section is reached. Further sample preparation is seen in section 3.3.

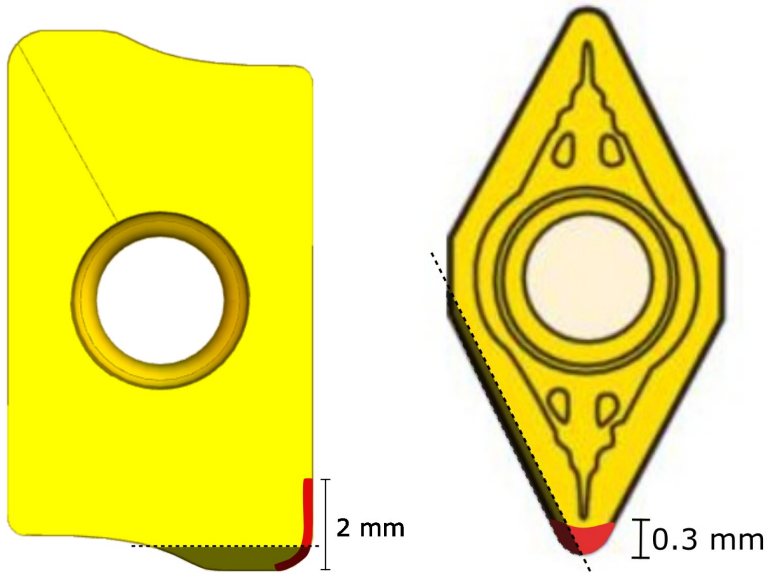

(a) (b)

Figure 13: Schematic image of the cross-section grinding. The faded area is ground away and the red area indicates the worn cutting edge. a) R390-11T308M-MM milling insert from Sandvik Coromant and b) DCMT11T304-F1 turning insert.

3.3 Sample preparation and microscopy

Both the diffusion couples and worn inserts are mounted in conductive Bakelite with carbon filler in order to be used in SEM. The samples were mounted in Polyfast using either a CitoPress-15 or Simpliment 2000, the worn inserts were held together with clamps during the mounting process. Once the samples were mounted, a Tegramin 30 polishing machine was used to polish the sample to a mirror finish. Due to numerous different samples and sample preparation locations, the polishing programs differed. For the Ti-5553/H13A 35 MPa sample silicon carbide grit papers P400 and P2500 were used for the initial polishing step, thereafter 6 µm and 3 µm diamond suspension on a neoprene surface for the final polishing step. The remaining diffusion samples and worn samples were polished with the following program seen in table 4. Depending on the polished surface on the last step the time is varied until a satisfied surface is reached.

The diffusion couple and worn insert samples were studied in a scanning electron microscope SEM, Tescan Mira3 FEG-SEM. An Oxford XEDS detector is also used for chemical characterization. Varied electron accelerating voltage is applied 10-15 kV depending on the purpose, for XEDS a higher accelerating voltage is used while imaging cavities a lower energy is utilized.

Table 4: Polishing sequence for the 2.5 GPa, 850 MPa, 0 pressure diffusion couples and worn insert samples using Struers Tegramin-30. (*) depending on the quality of the polished surface.

Surface	Application	Force (N)	Time (s)
Stuers MD-Piano 220	Water	20	30
Stuers MD-Plan	DiaPro All Lar. 9 μm + Water	15	120
Stuers MD-Nap	DiaDuo-2 1 μm + Water	10	240
Stuers MD-Chem	OP-U Non-dry + Water	5	300-600*

4 Results

4.1 Diffusion couples

4.1.1 Ti-5553/H13A and Ti-64/H13A ~ 0 pressure

The ~ 0 pressure diffusion couples were highly unreliable, for all samples except one the titanium and cemented carbide had difficulties diffusing into one another creating a poor bonding phase. The 1000 °C Ti-64/H13A sample was the only sample of which the titanium and cemented carbide had bonded together. An overview SE-SEM image is presented in figure 14a, between the insert and Ti-64 an intermediate layer is present which is shown in figure 14b. The intermediate layer is complex with both large cavities and brighter regions, the layer is approximately 25 µm. The interface between the cemented carbide and the intermediate layer is seen in figure 14c. Small voids <0.1 µm are present in the Co layer adjacent to the intermediate layer, these voids are infrequently found and sparse.

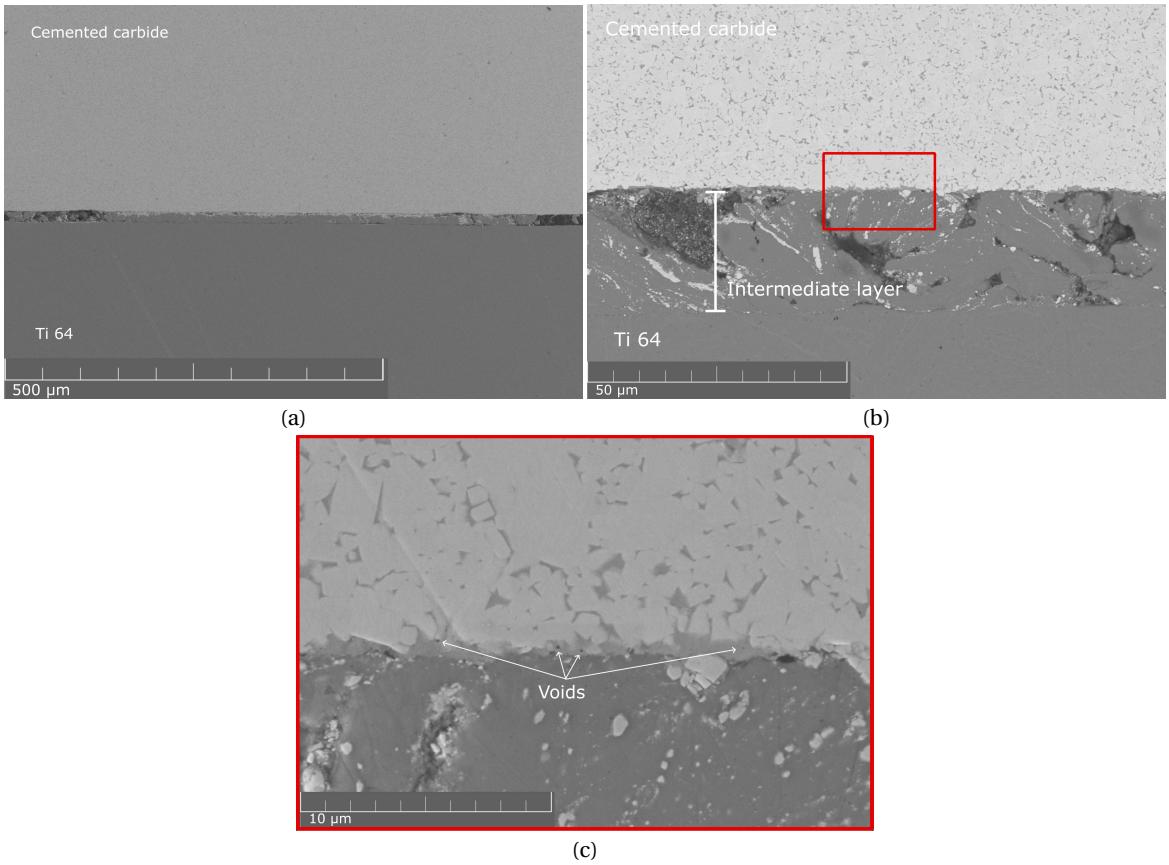

Figure 14: 1000 °C Ti-64/H13A ~ 0 pressure diffusion couple, a) overview SE-SEM image, b) BSE-SEM image showing the intermediate layer between the cemented carbide and the Ti-64. c) SE-SEM image of the interface between the cemented carbide and intermediate layer, voids are present in the cobalt layer adjacent to the interface.

The interface between the cemented carbide and the intermediate layer and EDS maps for Ti, W, C, Co, V and Al is shown in figure 15. From the Co XEDS map it is evident that the layer between the intermediate layer and the insert consist of Co, in this layer the small voids are found. The intermediate layer consist of Ti-64 with grains of possible WC or bcc W. Due to the nature of the intermediate layer, it seems contaminated

or something has gone wrong during annealing alternatively during sample preparation.

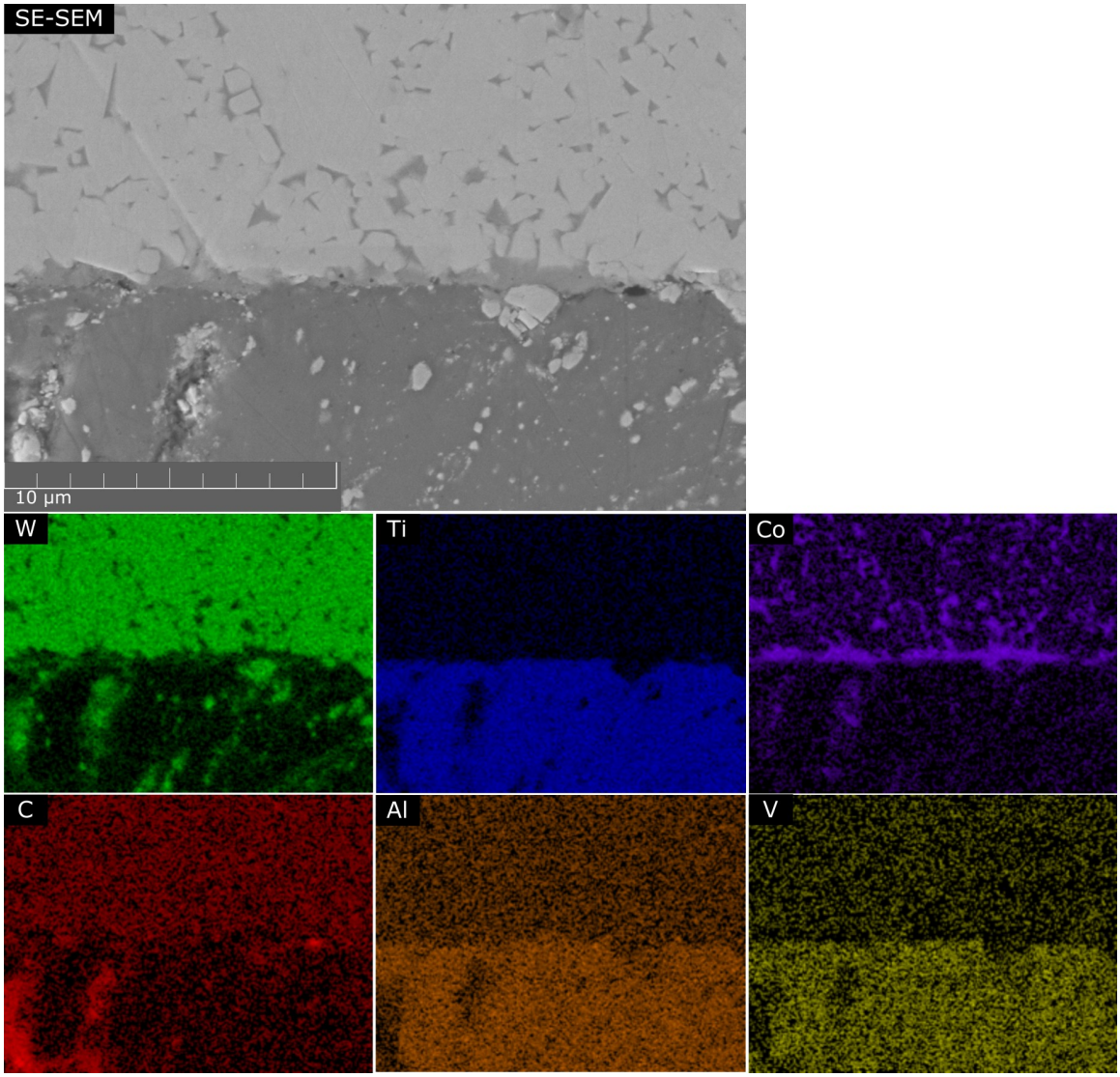

Figure 15: SE-SEM image of the interface between the cemented carbide and the Ti-64. XEDS maps for Ti, W, C, Co, V and Al is also included.

4.1.2 1200 °C Ti-64/cemented carbide 2.5 GPa and 1000 °C Ti-5553/H13A 35 MPa

This section presents both Ti-64/cemented carbide 2.5 GPa and Ti-5553/H13A 35 MPa diffusion couple together because the many similarities between the samples. Figure 16 displays an overview image of the diffusion couples.

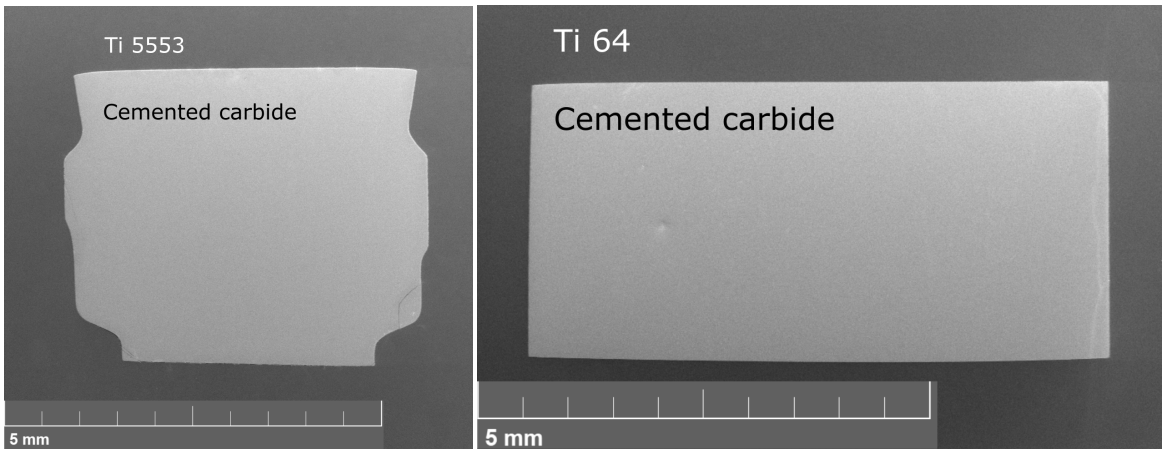

(a) (b)

Figure 16: Overview SE-SEM image of a) Ti-5553/H13A 35 MPa and b) Ti-64/cemented carbide 2.5 GPa diffusion couple.

In figure 17a Ti-5553/H13A 35 MPa diffusion couple is presented, in the cemented carbide two regions 1 and 2 are present. Region 1 is the WC grains with Co binder while in region 2 has instead a probable η-phase binder (M_6C/W_3Co_3C or $M_{12}C/W_6Co_6C$), this is not confirmed but likely based on earlier diffusion couple investigations presented in section 2.4.5. The WC grains are not as sharp and has more rounded edges in regions 2 compared to the grains in region 1 and the reference material in figure 10c. This suggests diffusion degradation, where W and C from the grains diffuses outwards from the grains. Throughout region 2 pores and cavities are present at various shapes and sizes <1 µm indicated by arrows in figure 17b. At the interface presented in figure 17c region 3 and 4 are present. From the XEDS result in figure 18 it is evident that region 4 is (Ti,V)C and region 3 W (bcc). Ti-5553 is indicated as region 5.

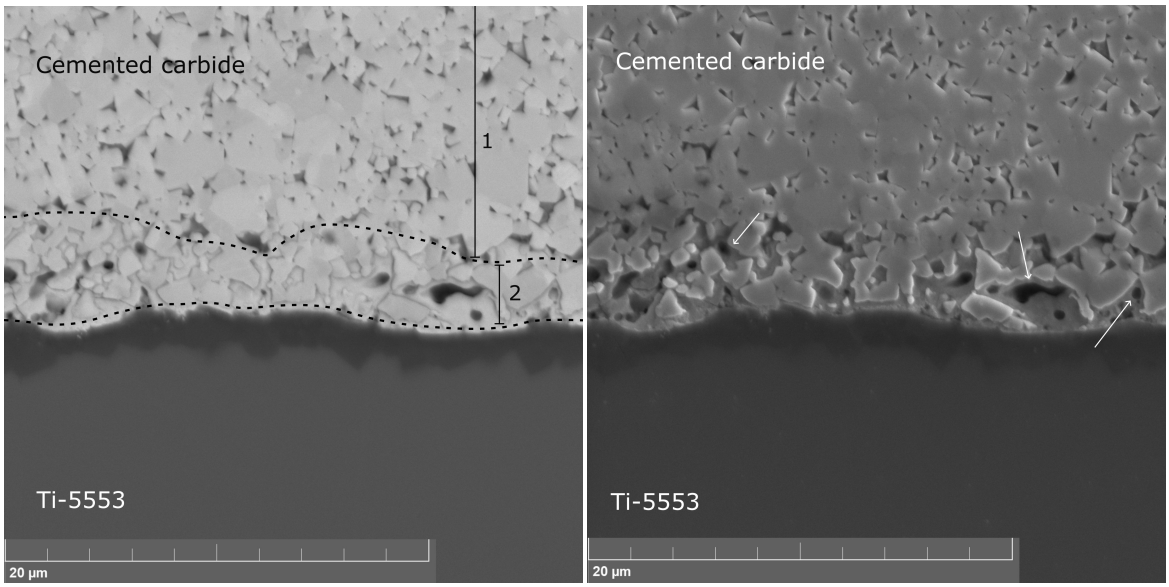

(a) (b)

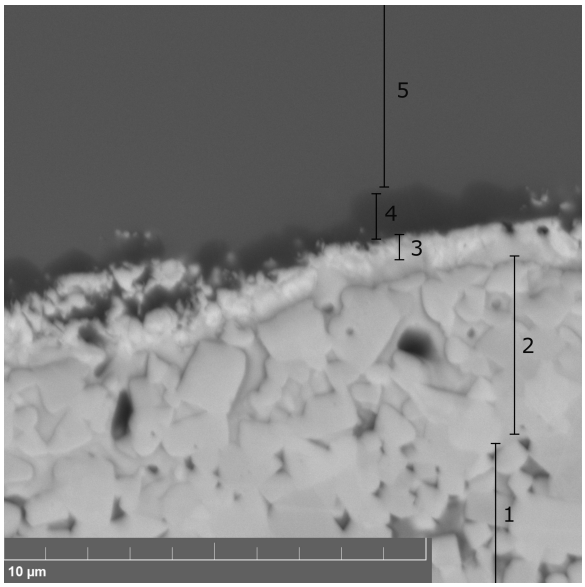

(c)

Figure 17: Ti-5553/H13A 35 MPa diffusion couple, a) BSE-SEM image showing region 1 and 2 in the cemented carbide where region 2 consist of a η-phase binder and region 1 Co binder. b) SE-SEM image indicating the pores seen in region 2 with arrows. c) BSE-SEM image of the diffusion couple interface presenting region 3, 4 and 5, region 3 is bcc W, 4 (Ti,V)C and region 5 Ti-5553.

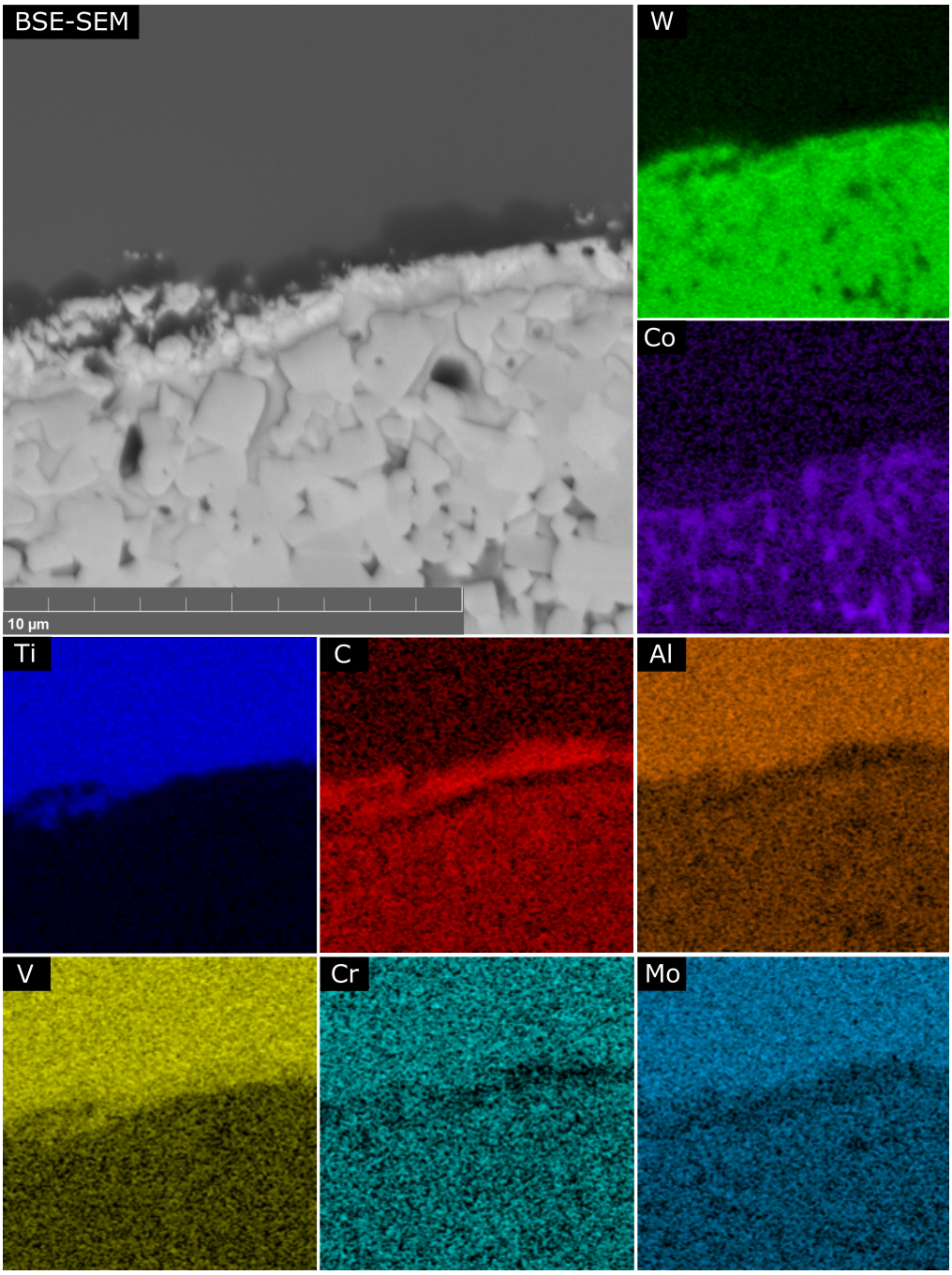

Figure 18: BSE-SEM image of the Ti-5553/H13A 35 MPa diffusion couple. XEDS maps for Ti, W, C, Co, V, Al, Cr and Mo is also included.

Throughout the cobalt binder in the cemented carbide darker cavities are present, see SE-SEM image in figure 19b which is 75 µm into the insert. These cavities are not as visual and large compared to the pores seen at the interface in figure 19a. The cavities are present throughout the WC-Co substrate with the size <0.25 µm.

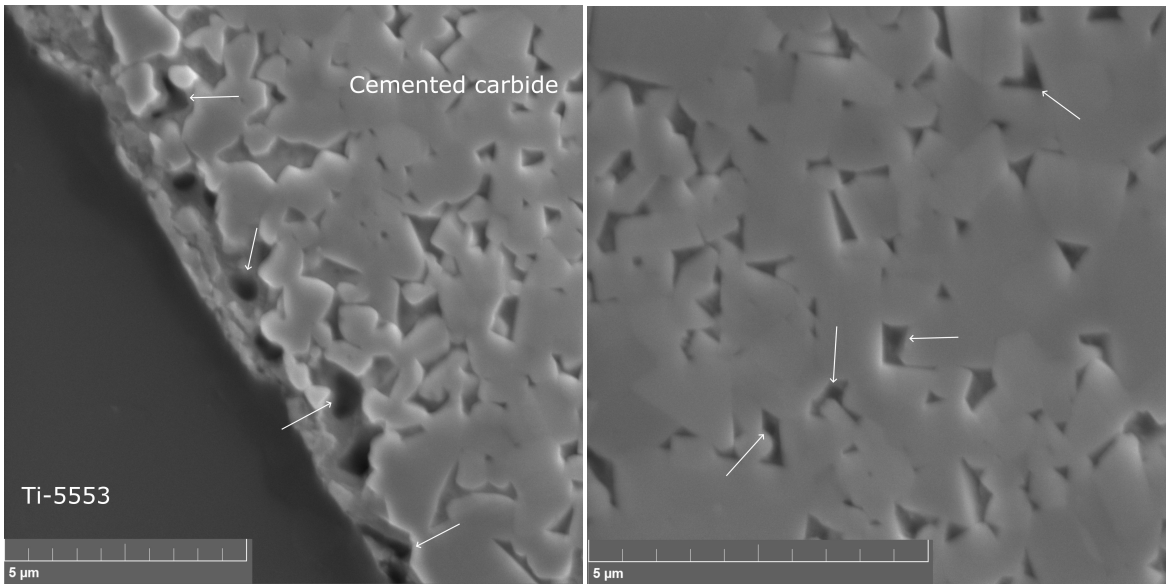

(a) (b)

Figure 19: SE-SEM images of Ti-5553/H13A 35 MPa diffusion couple, a) interface and b) cemented carbide bulk 75 µm into the insert.

In figure 20 the Ti-64/cemented carbide 2.5 GPa diffusion couple is presented, the diffusion couple appears to be identical with the Ti-5553/H13A 35 MPa diffusion couple. Similarly the cemented carbide has two distinct regions 1 and 2 where voids are present in region 2. It is assumed based on previous diffusion couple studies [5][30][55] that the binder in region 2 is η-phase. At the interface region 3 and 4 are also present which from XEDS data are concluded to be W and (Ti,V)C. The voids observed in the η-phase is shown in figure 20b, the voids are <µm and are only found close to the diffusion couple interface.

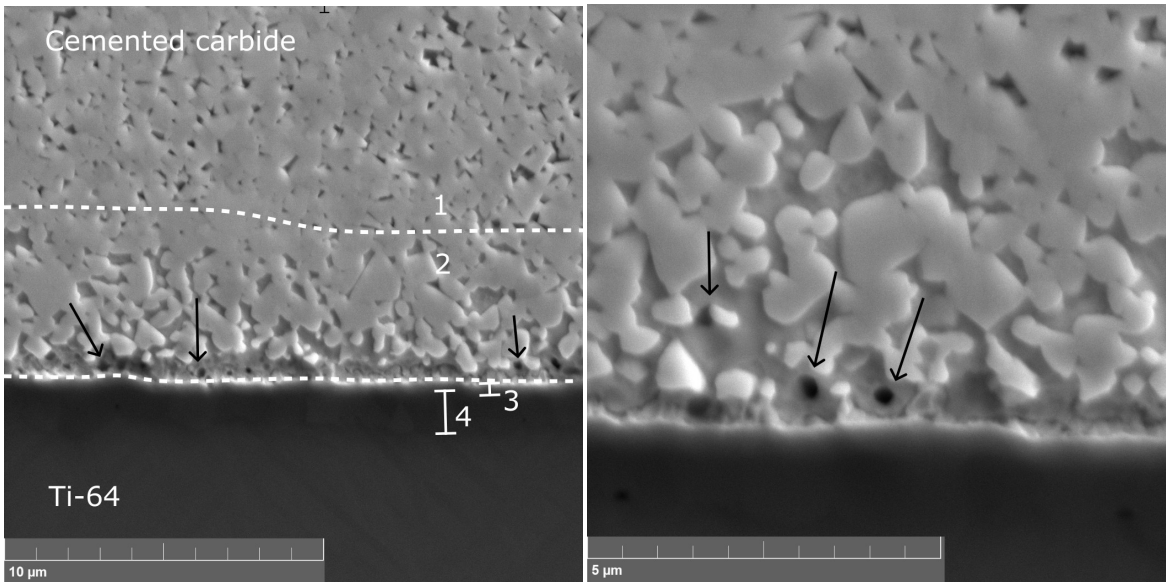

(a) (b)

Figure 20: SE-SEM images of Ti-64/cemented carbide 2.5 GPa diffusion couple, five regions are present. Region 1 WC with Co binder, region 2 WC with η-phase binder, layer 3 bcc W, layer 4 (Ti,V)C and the final region Ti-64. Voids are seen along the interface in the η-phase binder and highlighted by arrows.

4.1.3 1200 °C Ti-5553/H13A and Ti-64/H13A 850 MPa diffusion couple

The 1200 °C Ti-64/H13A 850 MPa diffusion couple is presented in figure 21a, a continuous crack is seen at the interface. BSE-SEM image of the interface is illustrated in figure 21b, several phases are present in between the two diffusion couple substrates. The Ti-64 closer to the interface consist of more β-phase strengthened Ti in comparison to further into the bulk where the Ti-64 is unaffected by chemical interaction with the tool. The dark regions indicated by arrows in the Ti-64 is seen along the diffusion couple interface and at various sizes at around 20 µm, these regions are only found at the interface and not in the Ti-64 bulk. On the cemented carbide side there are two distinct regions, region 1 which is seen from 15 µm and further into the bulk and region 2 adjacent along the interface. Region 1 is WC grains with Co binder while region 2 is most likely WC grains with η-phase binder. At the bonding interface three different regions are present in figure 21c, together with XEDS result shown in figure 22 region 4 depicts a solid solution of dark (Ti,V)C and bright W (bcc). Region 5 consist of a mixture of dark β-phase strengthened Ti and lighter bcc W. Region 3 is presented with SEM image in figure 21d and XEDS result in figure 23, it is evident that this bright band corresponds to bcc W. In region 3 small voids are present in the W grains, in region 1 and 2 no voids or pores are observed. In region 5 and below inside the β-phase strengthened Ti void are present at various size <0.5 µm.

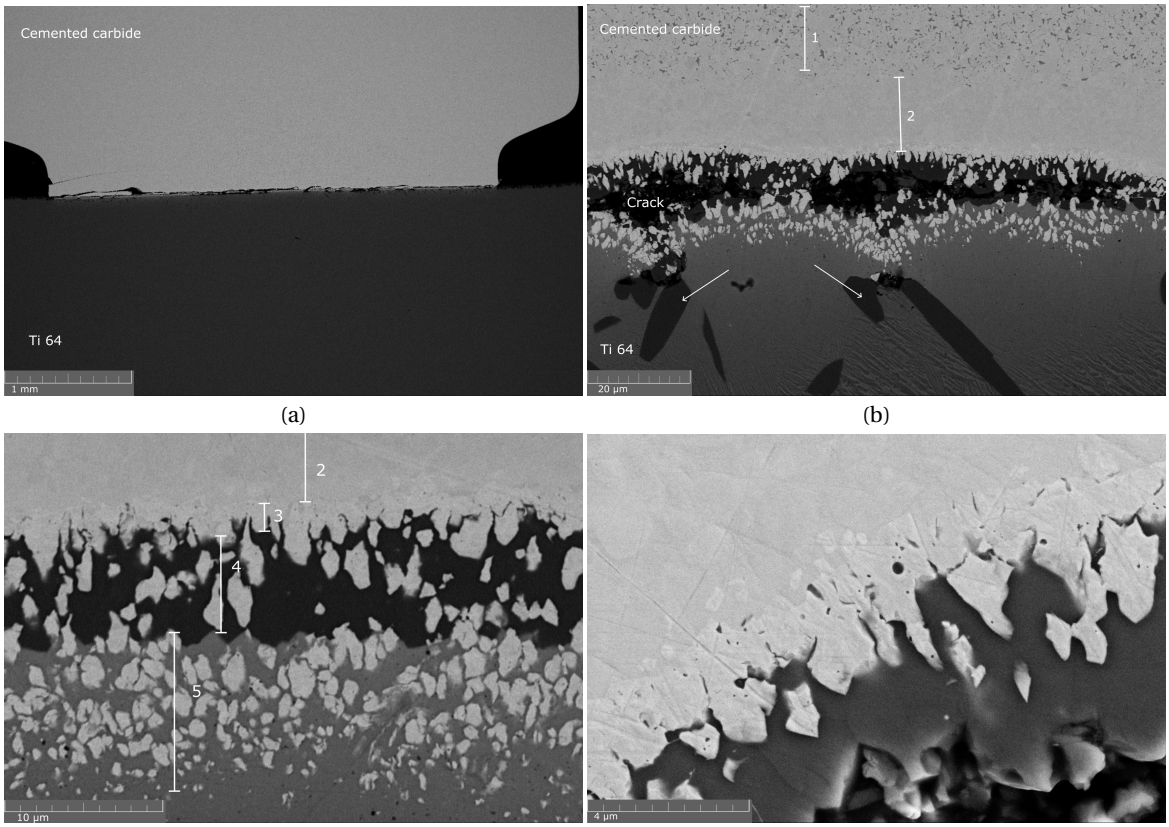

Figure 21: 1200 °C Ti-64/H13A 850 MPa diffusion couple, a) overview BSE-SEM image showing cracks along the interface. b) BSE-SEM image showing the diffusion bond where the tool has two evident regions 1 and 2, the arrows indicate dark patches in the Ti-64. c) BSE-SEM image of the diffusion couple interface three region bands are present. Region 3 contist of bcc W, region 4 bcc W and (Ti,V)C and region 5 a mixture of dark β-phase strengthened Ti and bright bcc W. Voids are observed in the β-Ti. d) SE-SEM image presenting region 3 which has small voids or cavities.

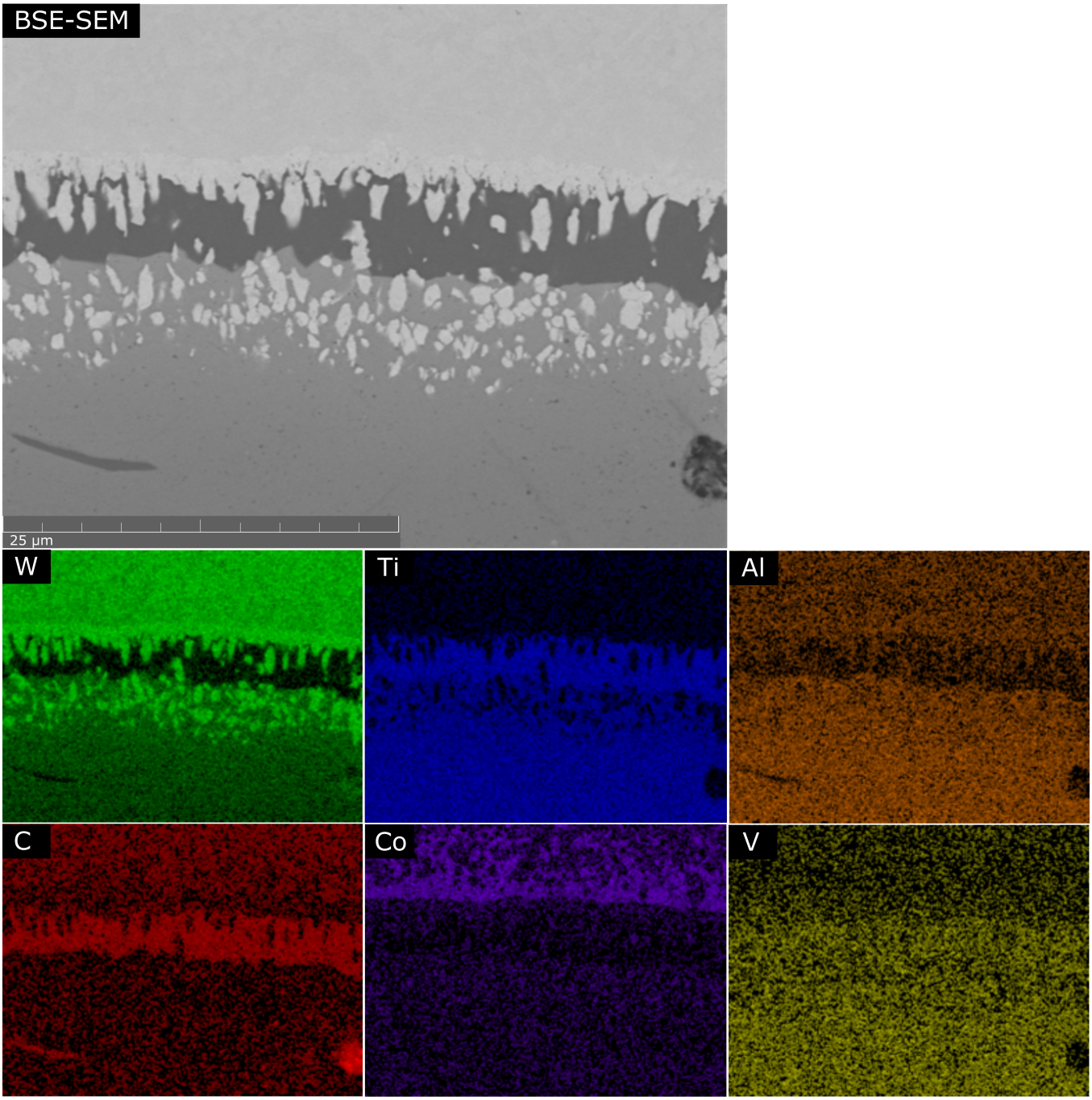

Figure 22: BSE-SEM image of the interface between the 1200 °C Ti-64/H13A 850 MPa diffusion couple. XEDS maps for Ti, W, C, Co, V and Al is also included.

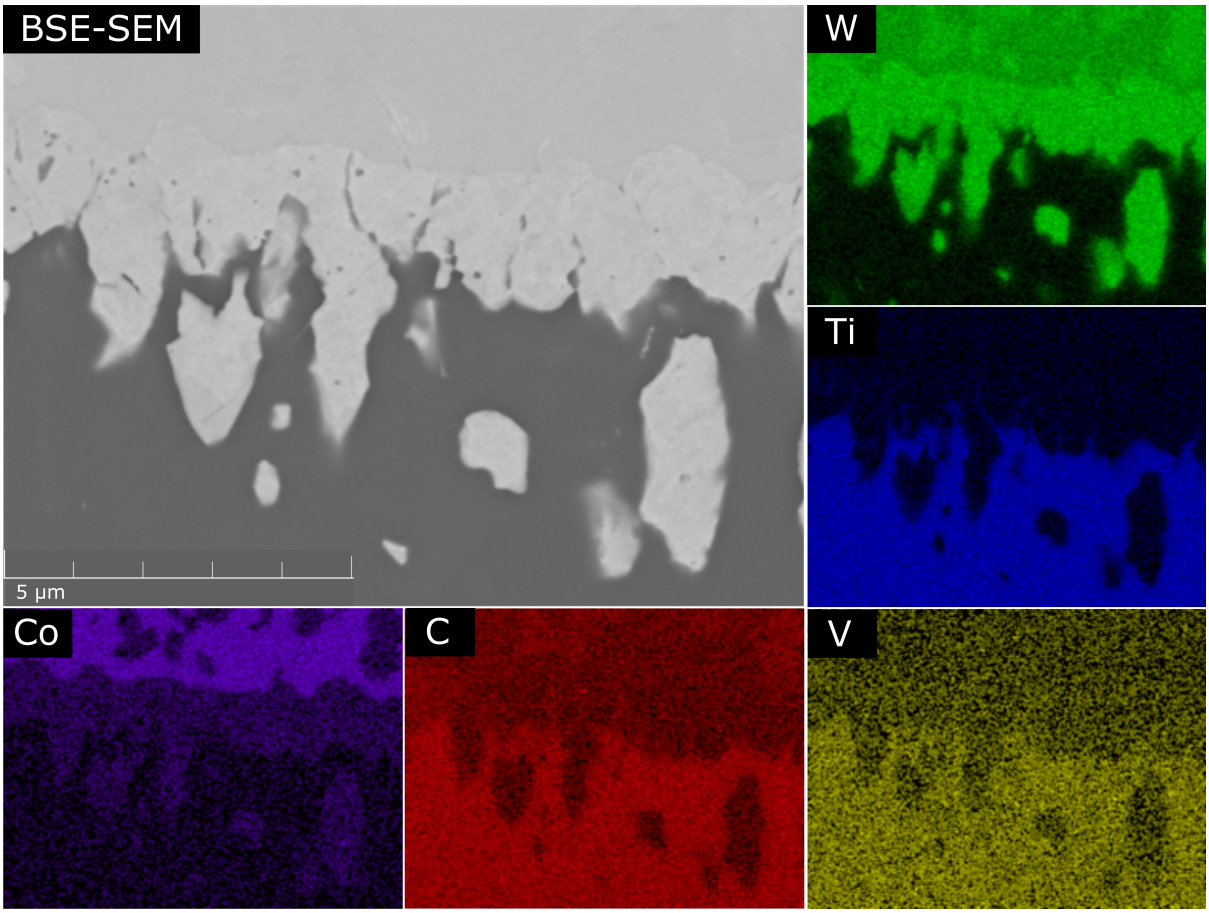

Figure 23: BSE-SEM image of region 3 depicted in figure 21c. XEDS maps for Ti, W, C, Co and V is also shown.

Similar to the Ti-64 the 1200 °C Ti-5553/H13A 850 MPa diffusion couple has a resembling diffusion bond, presented in figure 24a. A pervading crack throughout the diffusion interface is observed and dark regions in the Ti-5553 is observed but not as recurrent as in Ti-64. In figure 24b, voids in the Ti-5553 adjacent to the interface are present, similar voids are seen in the bcc W layer shown in figure 24c. Region 1 and 2 which is seen in the Ti-64/H13A 850 MPa diffusion couple is also present with Ti-5553 sample, throughout these regions no voids or cavities are seen.

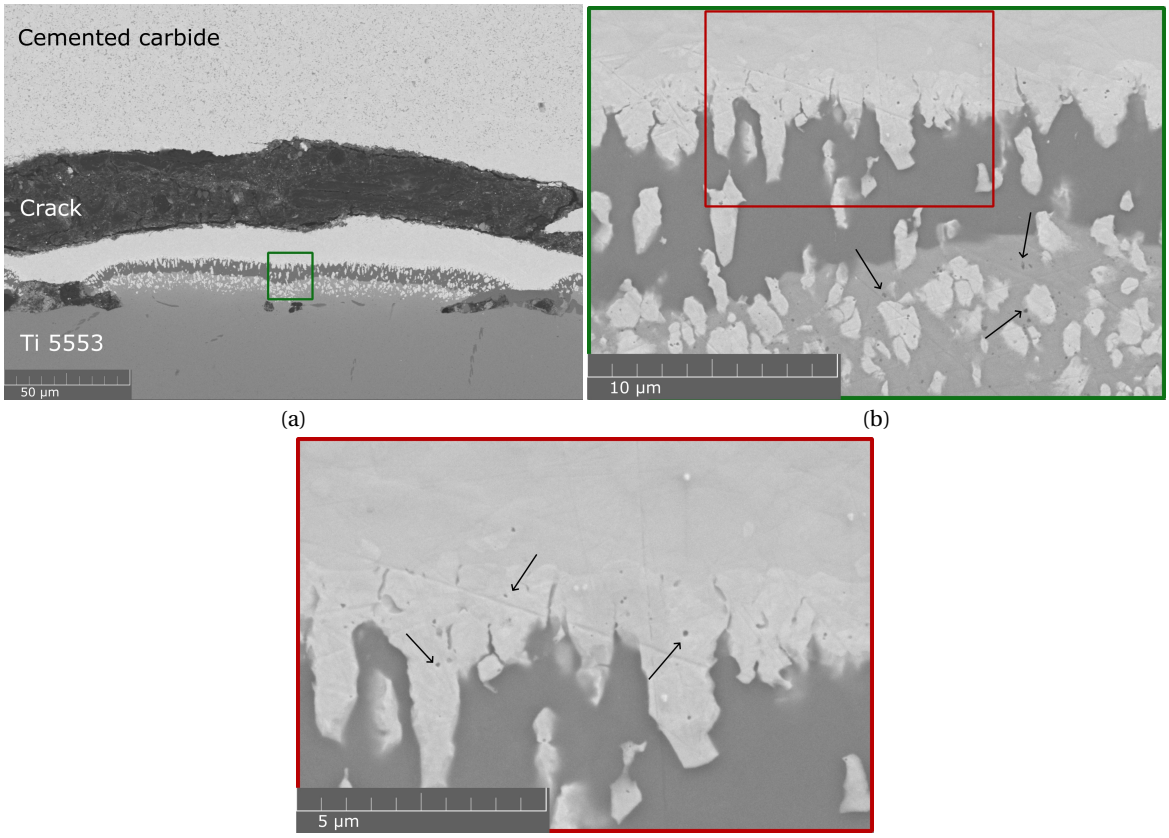

(a) (b)

(c)

Figure 24: 1200 °C Ti-5553/H13A 850 MPa diffusion couple, a) overview BSE-SEM image showing crack along the interface. b) SE-SEM image showing the diffusion bond with arrows indicating voids in the Ti-5553. c) BSE-SEM image of voids indicated by arrows in bcc W layer.

4.1.4 1000 °C Ti-5553/H13A and Ti-64/H13A 850 MPa diffusion couple

The 1000 °C Ti-5553/H13A 850 MPa diffusion couple had cracks along the diffusion interface with no pronounced regions of diffusion bond with the tool and workpiece material, therefore this sample is dismissed.

The 1000 °C Ti-64/H13A 850 MPa diffusion couple is presented in figure 25. Similar to the 1200 °C diffusion couples the Ti-64 consist of gradually more β-Ti closer to the interface. The regions seen in the 1200 °C samples are also observed, region 2 with WC and η-phase mixture is thinner and no voids are observed. Similarly voids are found in the β-Ti adjacent to the interface and in the bcc W layer at the interface.

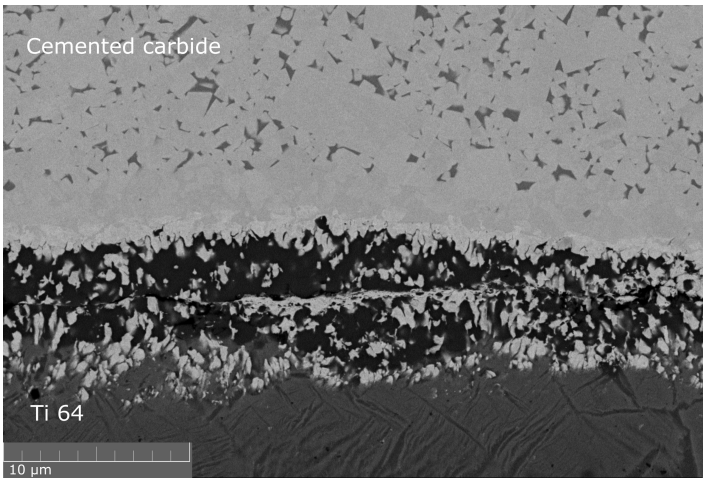

Figure 25: BSE-SEM images of the 1000 °C Ti-64/H13A 850 MPa diffusion couple.

4.1.5 800 °C Ti-5553/H13A and Ti-64/H13A 850 MPa diffusion couple

The 800 °C Ti-5553/H13A 850 MPa diffusion couple is presented by SEM images in figure 26a, the diffusion couple had a poor diffusion bond with predominant cracks and cavities between the cemented carbide and titanium, only in a few regions the diffusion couple is bonded. One of these regions is seen in figure 26b, both the Ti-5553 and cemented carbide seems unaffected and has not reacted with one another. Along the adjacent Co layer closest to the Ti small voids <0.1 µm are found infrequently and sparse. The Ti-5553 microstructure and the distribution of the $\alpha$and β-Ti at the diffusion couple interface and Ti-5553 bulk are equal.

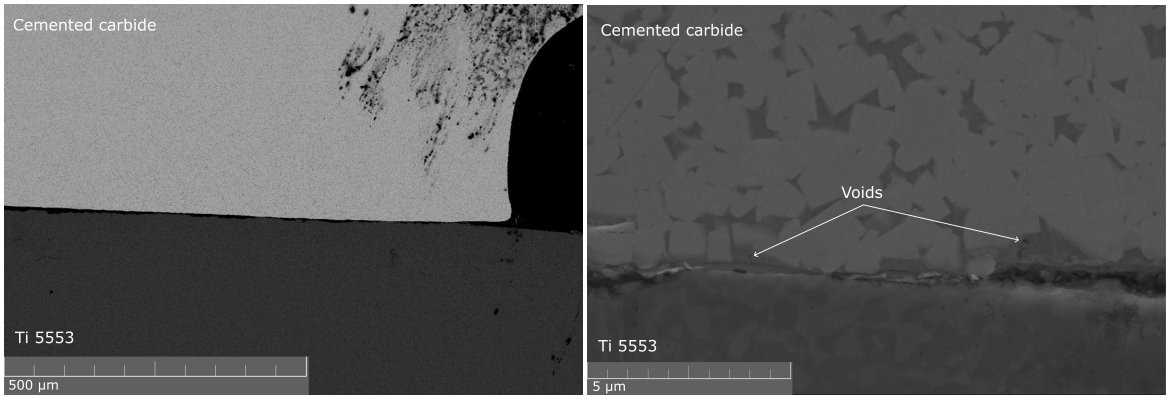

(a) (b)

Figure 26: a) BSE-SEM overview image and b) SE-SEM image of Ti-5553/H13A 850 MPa diffusion couple interface. Small voids are found in the cobalt layer adjacent to the Ti.

Similarly the 800 °C Ti-64/H13A 850 MPa diffusion couple has poor diffusion bond with predominant cracks and cavities along the interface as seen in figure 27a. Unlike the Ti-5553 diffusion couple no small voids are found in the Co layer, see figure 27b.

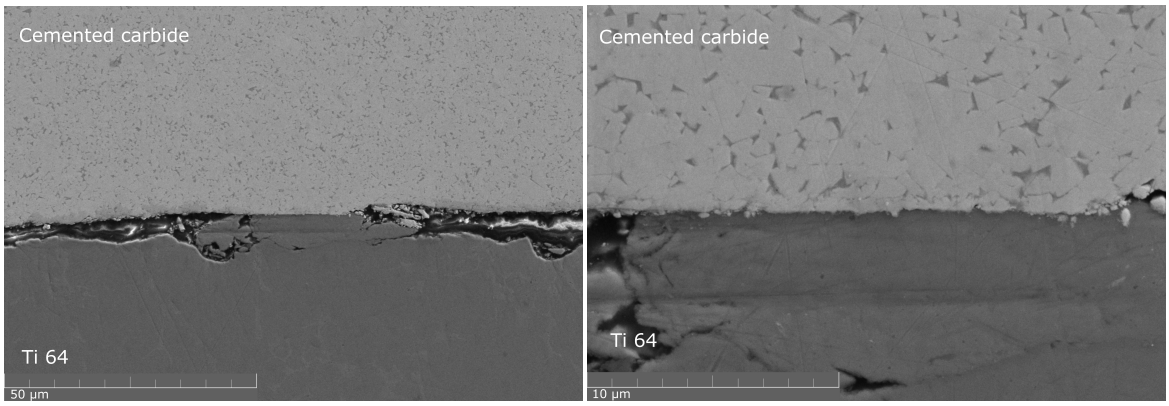

(a) (b)

Figure 27: SE-SEM images of the 800 °C Ti-64/H13A 850 MPa diffusion couple interface.

The interface between the cemented carbide and the Ti layer for the 800 °C Ti-64/H13A 850 MPa diffusion couple and XEDS maps for Ti, W, C, Co, V and Al is shown in figure 28. It is evident from the EDS result that no new phases are formed in the diffusion interface, both the Ti-64 and CC seems unaffected by the diffusion couple process. WC particles are found In the Ti-64, this is most likely a result from the polishing process where small WC grains are broken off and adhered to the softer Ti-64.

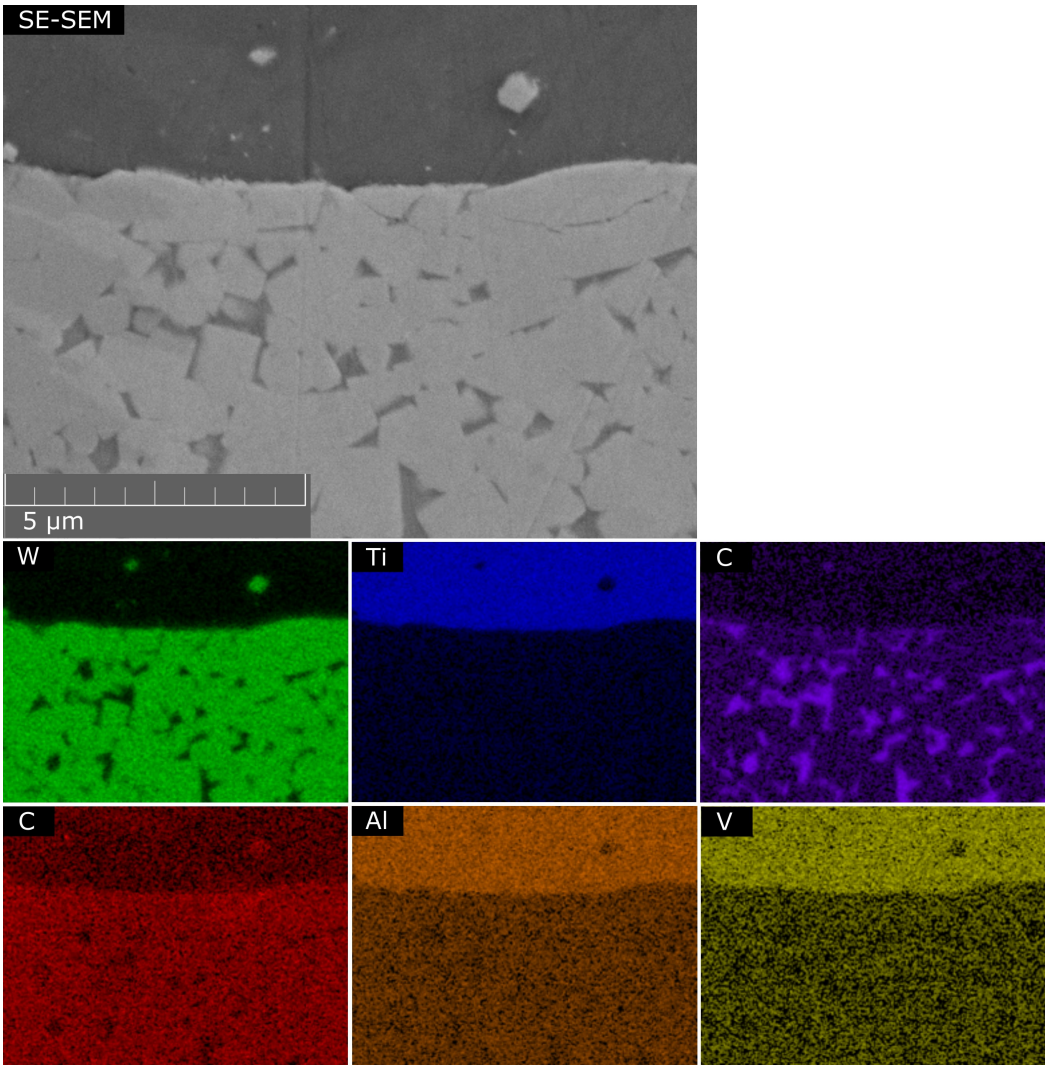

Figure 28: SE-SEM image of the diffusion interface of the 800 °C Ti-64/H13A 850 MPa diffusion couple. XEDS maps for Ti, W, C, Co, V and Al is also included.

4.2 Worn milling inserts - M1, M2 and M3

Figure 29 shows SEM overview images of M1, M2 and M3 worn inserts, both the rake and flank are worn and Ti-64 has adhered to the cemented carbide. All inserts has no distinct crater wear and cracks are present in the M1 insert, all inserts have fractured at several regions at the cutting edge. The red square region seen in the M2 insert is less worn compared to other areas, here Ti-64 has adhered. The M3 insert has residual debris on the Bakelite, it is believed to be from the clamps used during mounting the inserts. The outline of an unworn insert is drawn for the M1 and M2 inserts.

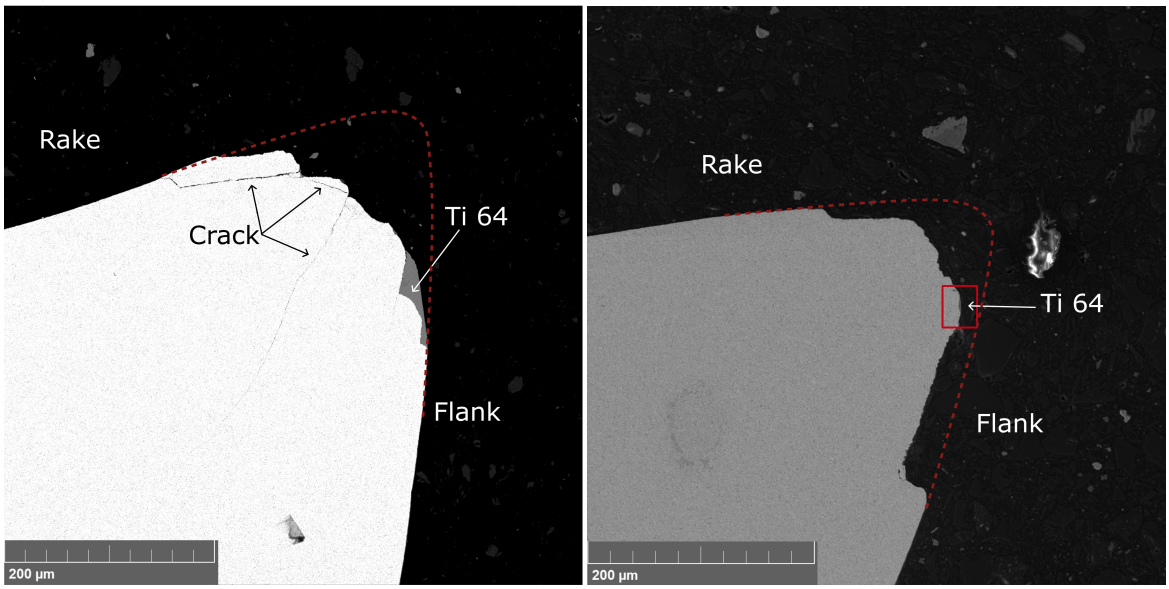

(a)

(b)

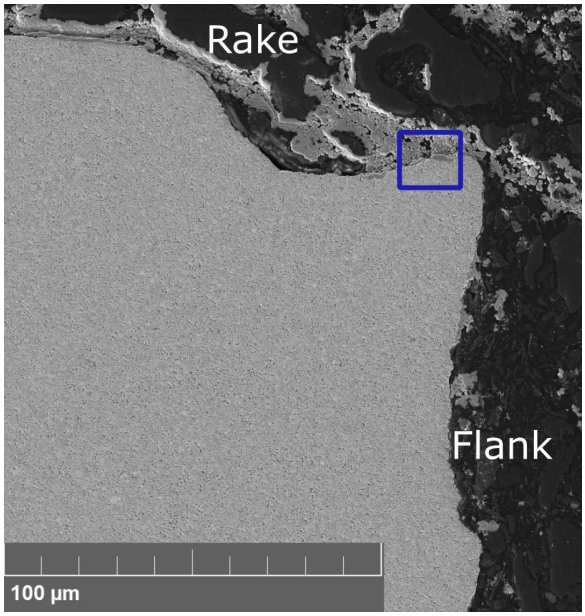

(c)

Figure 29: SEM overview image of a worn milling insert a) M1, b) M2 and c) M3. Adhered Ti-64 on the cutting edge is indicated, outline of a unworn insert is drawn for insert M1 and M2.

4.2.1 M1

The cutting edge of the worn M1 insert is seen in figure 30, all regions has adhered Ti 64 at the insert interface and no voids or darker regions are present in the cobalt binder.

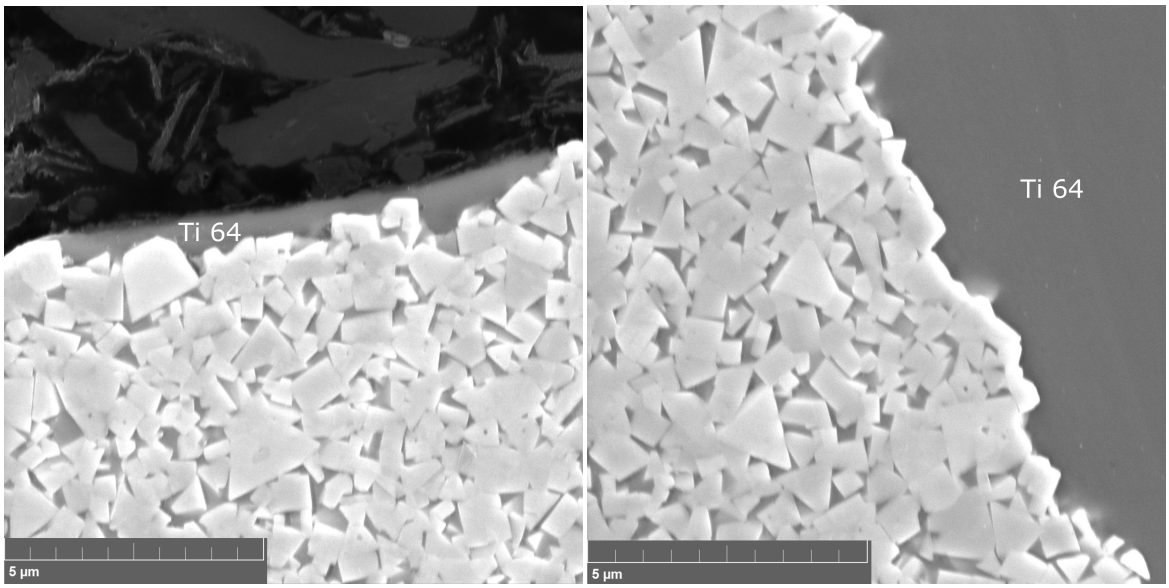

(a) (b)

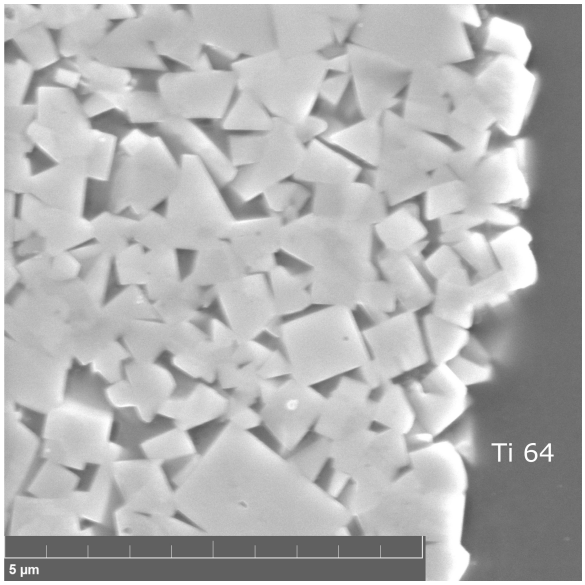

(c)

Figure 30: SE-SEM images of the worn M1 insert. Ti-64 has adhered to the cemented carbide and there are no evident voids or darker regions present in the cobalt binder.

4.2.2 M2

SE-SEM images from the red square region in figure 29b is presented in figure 31, Ti-64 has adhered to the cemented carbide. Darker regions are present in the cobalt binder and could possibly be cavities, the darker regions are only seen from the interface to 15 µm into the cemented carbide. The darker features are shown by arrows and are of irregular rounded shape and found only in the binder phase along the WC/Co interface, the cavities are <0.5µm in size. Since the SE-SEM image showed a more defined contrast of the darker patches while the BSE-SEM images are more diffuse, the surface sensitive SE-SEM image indicate that they are indeed voids. The voids occupy ~ 0.43% of the area in the cemented carbide, this is calculated

by measuring the area of the voids divided by the total area in which voids are observed.

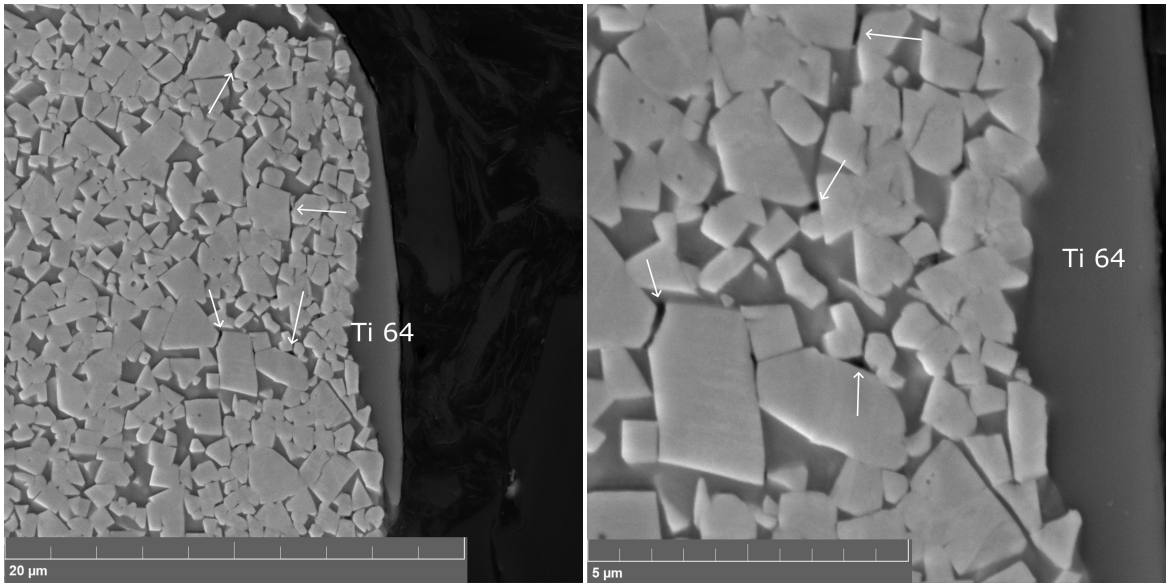

(a) (b)

Figure 31: SE-SEM image of the worn M2 tool in the red square region in figure 29b, adhered Ti-64 is seen at the cemented carbide interface. Arrows indicate cavities in the cobalt binder phase along the WC/Co interface.

.

At regions alongside the red square region which are more worn are presented in figure 32. No adhered Ti-64 is present and neither dark areas in the cobalt binder.

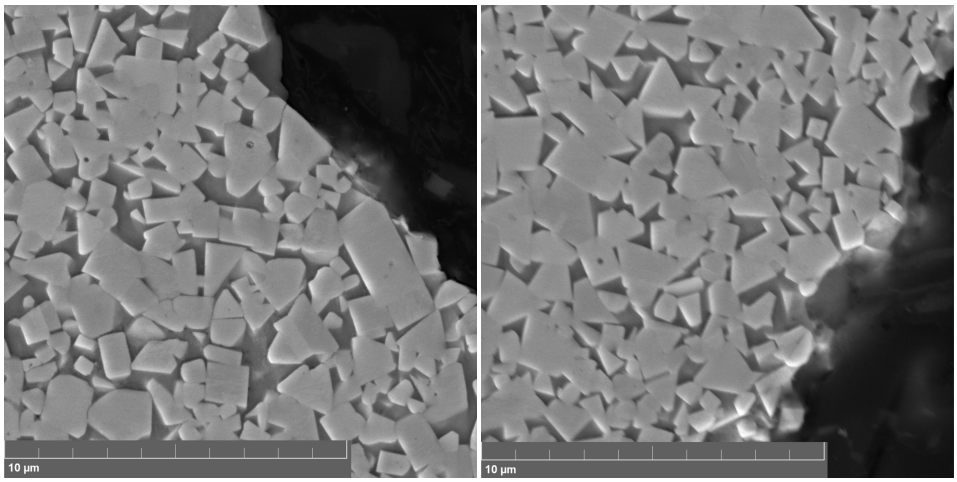

(a) (b)

Figure 32: SE-SEM image of the worn M2 tool, a) rake and b) flank side. No adhered Ti-64 is present and neither any darker regions in the cobalt binder phase.

4.2.3 M3

Along the cutting edge of the worn M3 insert groups of voids are present at several regions, see figure 33 from the blue square in figure 29c. The groups of cavities are of irregular shape and in the Co binder. At the cutting edge no adhered Ti-64 is evident.

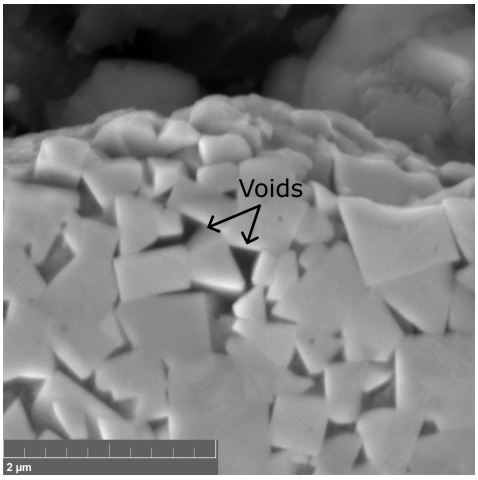

Figure 33: SE-SEM image of the worn M3 insert at the blue square region in figure 29c, a group of voids are indicated.

4.3 Worn turning insert - T1

Figure 34a and b presents BSE-SEM overview images of the worn turning insert. Both flank and crater wear is noticeable and adhered Ti-64 is seen both on the flank and crater. Figure 34c, d and e shows the crater, bulk and flank interface. Arrows indicate darker regions in the cobalt binder which can be seen in the cemented carbide at the flank, crater and bulk. These darker regions are potentially cavities within the insert.

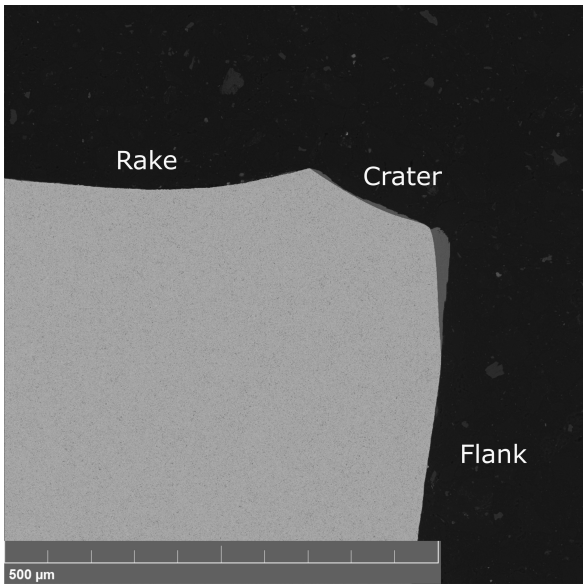

(a)

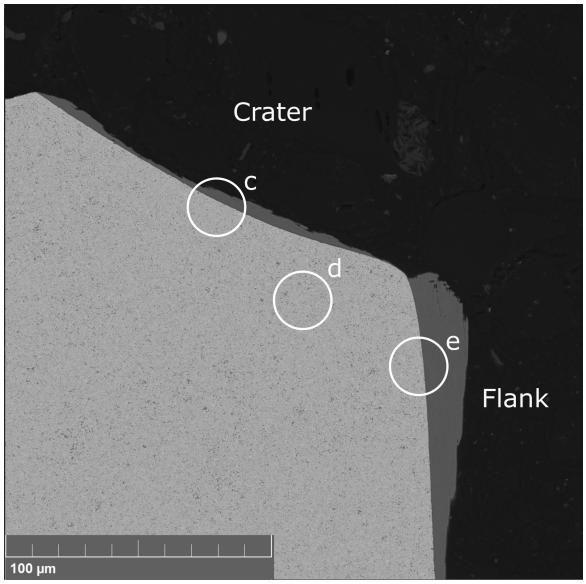

(b)

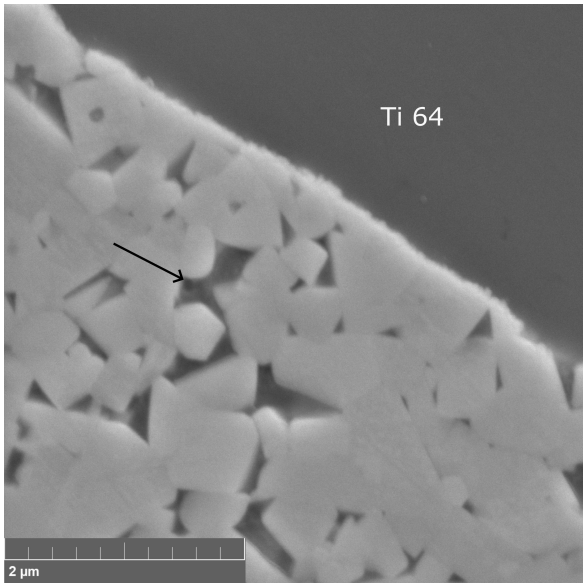

(c)

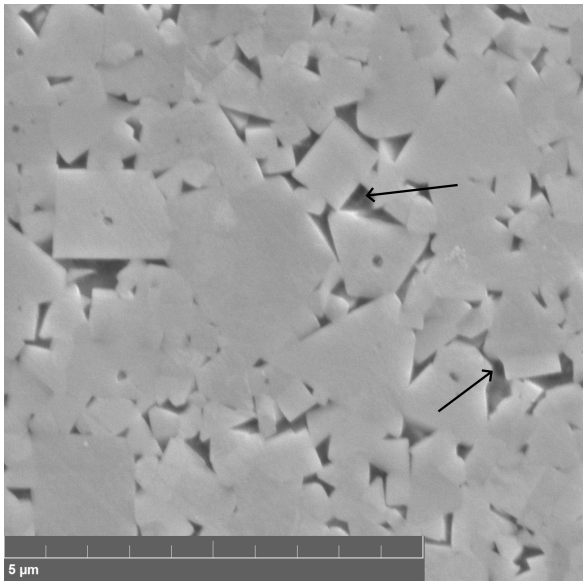

(d)

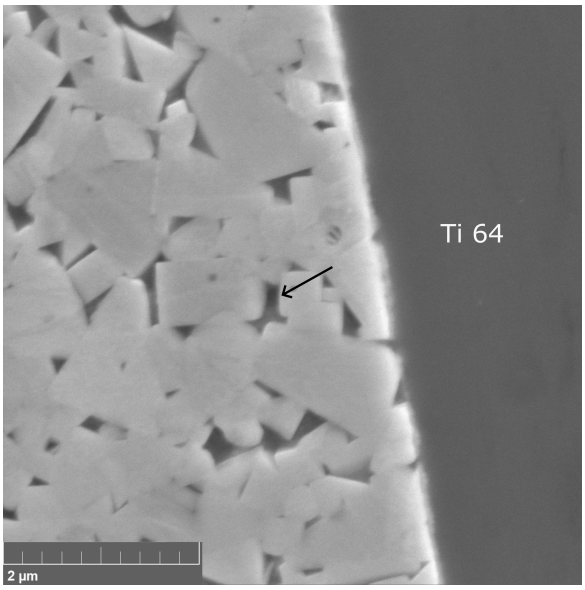

(e)

Figure 34: a) and b) BSE-SEM overview image of worn insert, adhered titanium is seen on the flank and crater. SE-SEM image of the worn insert at the c) crater, d) bulk and e) flank. The arrows indicate darker regions in the cobalt binder.

5 Discussion

The aim of the study is to investigate the possibility of Kirkendall porosity during Ti-5553 and Ti-64 machining. The thesis is that Co binder diffuses at a faster rate to the workpiece material compared to Ti diffusing inwards. The diffusion rate difference would result in a net movement of vacancies into the binder phase resulting in nucleation of voids, known as Kirkendall pores. The difference in diffusion or permeability is a requirement for Kirkendall pore formation. From the theory, it is apparent that the diffusion ratio between Co diffusion in Ti and Ti diffusion in Co is more than three orders of magnitude at the interesting temperate range 800-1200 °C. The big difference between diffusion coefficients is a requirement for Kirkendall porosity. The permeability of Co in Ti-5Al5V is calculated at 1000 °C, the permeability is calculated by mobility times solubility [5]. The solubility of Co in Ti is relatively high at 1000 °C and the Ti is constantly replenished during machining. The solubility of Ti in Co at 1000 °C is less than the solubility of Co in Ti [56], which further supports that Kirkendall porosity is possible during titanium machining.

The Kirkendall porosity explanation in the Ti/Co system has one issue, since the voids form due to accumulations of vacancies the diffusion mechanism has to be substitutional. It is believed that Co diffusion in both β and α-Ti is interstitial and not substitutional, if that is the case the Kirkendall porosity would not be possible. However, after a discussion with my supervisors, the interstitial diffusion mechanism of Co in Ti is unreliable and unreasonable [41]. Kirkendall porosity in Ti machining is still open for discussion and likely to occur during titanium machining.

5.1 Diffusion couples

5.1.1 Ti-5553/H13A and Ti-64/H13A ~ 0 pressure

The ~ 0 pressure diffusion couples which imitates the conditions at where the chip breaks contact with the insert. Unfortunately, these samples did not form a strong diffusion bond during the annealing process, a more suitable process would be to slightly pin the diffusion couple together with either a clamp or with the

force of a weight. The 1000 °C Ti-64/H13A sample that formed a diffusion bond had a surprising intermediate layer seen in figure 14b. The explanation for this layer is unclear, however the bright patches of WC are probably broken off WC grains which occurred during polishing. No other phases such as TiC or η-phases are present which does not correspond with previous diffusion couples. The small voids in the Co layer adjacent to the intermediate layer as shown in figure 14c could be Kirkendall pores, since they are sparse, infrequently found and the uncertainty of the intermediate layer no conclusion of these voids can be made.

5.1.2 1200 °C Ti-64/cemented carbide 2.5 GPa and 1000 °C Ti-5553/H13A 35 MPa

The two diffusion couples have the same order of phases, first WC/Co, second WC/η-phase, third a thin layer of bcc W, fourth a layer of (Ti,V)C and last a Ti-64 or Ti-5553 microstructure. Both the 1200 °C Ti-64/cemented carbide 2.5 GPa and 1000 °C Ti-5553/H13A 35 MPa has sufficiently large voids in the η-phase binder. How are these voids formed during the annealing process? The hypothesis that Kirkendall porosity is the cause is difficult to argue. Since there are three regions amidst the Co binder and the Ti, a (Ti,V)C, W and η-phase layer. The Co and Ti diffusion coefficients in these layers are mostly unknown. Although the Ti self-diffusion in TiC is extremely slow, TiC is a diffusion barrier for Ti [57]. The high pressure during the annealing of the 1200 °C Ti-64/cemented carbide 2.5 GPa sample is not enough to suppress the nucleation and growth of the cavities. Since cavities are formed in this high pressure diffusion sample it is reasonable in future studies to look for pores at the rake face, along the high pressure region where the chip compresses against the insert. In the pressurized examples mentioned in section 2.5.4, 9 and 14 MPa prevents Kirkendall porosity. These diffusion couples included softer metals such as Cu, Nb and Ni, therefore it is believed that the hard WC-grains in the insert support and stabilize the possible Kirkendall void formation at high pressure.

The small cavities in Co binder of sample 1000 °C Ti-5553/H13A 35 MPa shown in figure 19 are probably not created during annealing. This is due to the fact that the cavities are observed in the bulk material, not only at the cutting edge. The reason for the voids are indecisive but they could arise during the polishing step or they are created throughout the insert manufacturing.

5.1.3 1200, 1000 °C Ti-5553/H13A and Ti-64/H13A 850 MPa diffusion couple

These samples had a uniform appearance except the 1000 °C Ti-5553/H13A diffusion couple as it had no diffusion bond. The different phase layers are as follows, first WC-grains with Co binder, second WC-grains with η-phase binder, third bcc W, fourth (Ti,V)C, fifth bcc W with β-Ti and last the Ti with a higher concentration of β-Ti closer to the interface. The layers are shown in figure 35a. Similar layers are observed in Fieandts et al.[30] commercially pure Ti/H13A diffusion couple shown in figure 35b. In Hatts et al. [55] Ti-64/H13A diffusion couple matching layers are evident in figure 35c. Both these papers did not report any cavities in the η-phase, neither was there any in the 1200, 1000 °C Ti-5553/H13A and Ti-64/H13A 850 MPa diffusion couples. However it is evident that both Co and W has diffused into the Ti, this is evident from the XEDS data and the high fraction of β-Ti near the diffusion interface. The Co and W are both β-Ti stabilizing elements.

The Co diffusion is a requirement for Kirkendall porosity, however voids are not observed in the insert. A possible explanation could be that the (Ti,V)C and bcc W layer delay the Co diffusion, therefore the insert does not get supersaturated of vacancies and no nucleation of voids can form. However this theory has complications, the 1200 °C Ti-64/cemented carbide 2.5 GPa and 1000 °C Ti-5553/H13A 35 MPa in which voids are observed has both (Ti,V)C and bcc W layers. An explanation can be the ramp rate during the annealing process seen in figure 11. At lower ramp rates for the 850 MPa, Hatts and Fieandts sample the barrier layers form at lower temperatures before the Co has a high diffusion rate. When the diffusion couple reaches holding temperature the diffusion barriers are already formed and the Co diffusion is retarded. For the 1200 °C Ti-64/H13A 2.5 GPa and 1000 °C Ti-5553/H13A 35 MPa sample the heating ramp rates are high, therefore the diffusion barrier layers are thin when holding temperature is reached. At the holding temperature the Co diffusion is not delayed and Kirkendall voids can form, this happens until thicker diffusion barriers are

formed.

The diffusion couple experiment is not an optimal method to study if diffusion causes pores in the insert, since new diffusion barriers are formed during annealing such as (Ti,V)C, bcc W and η-phase. A diffusion couple without the stagnant layers would be beneficial, however, how this diffusion couple will be constructed is unknown.

The dark patches in the Ti observed in 1200 °C Ti-5553/H13A and Ti-64/H13A diffusion couples are probably TiC. These are not studied further during the XEDS analysis, however similar dark features have been confirmed to be TiC [58]. The origin to the small voids found in the bcc W layer is unknown, moreover, the cause of the voids found in the β-Ti is also undetermined.

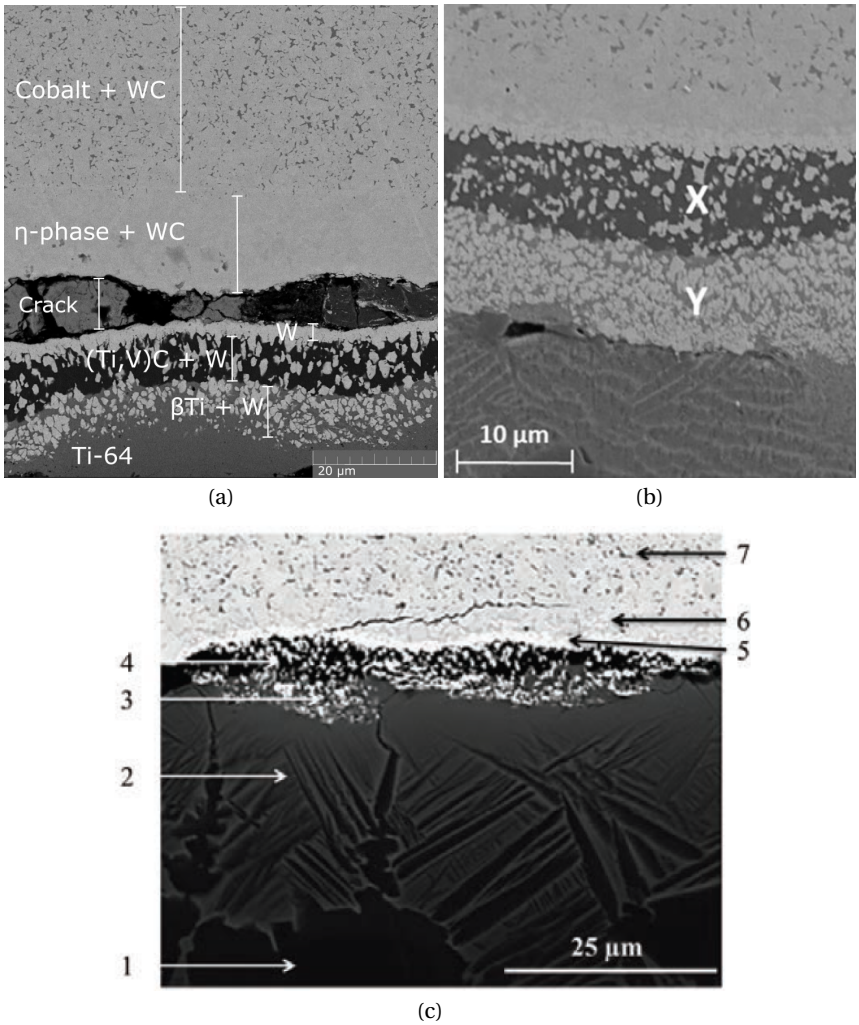

(a) (b)

(c)

Figure 35: SEM images of a) 1200 °C Ti-64/H13A 850 MPa diffusion couple indicating the different layers, b) commercially pure Ti/H13A diffusion couple by Fieandt et al. [30] and c) Ti-64/H13A diffusion couple by Hatt et al. [55].

5.1.4 800 °C Ti-5553/H13A and Ti-64/H13A 850 MPa diffusion couple

The poor diffusion bond in the diffusion couples and no new phases such as (Ti,V)C or η-phase is observed which indicates little to no diffusion during the annealing process. This is further strengthened by the fact

that the Ti-5553 distribution of α and β-Ti at the diffusion couple interface and Ti-5553 bulk is equal. Since Co and W are β-Ti stabilizing and no increase of β-Ti is seen at the diffusion interface, no outwards diffusion of Co and W is concluded. The small, infrequent and sparse voids found in the Ti-5553/H13A diffusion couple are inconclusive, they are probably not caused by the Kirkendall effect since little diffusion is observed and the voids are sparse.

5.2 Worn inserts

5.2.1 T1

The worn turning insert has small darker regions/spots in the Co binder, these features are possible perceived as cavities. From the result the cavities are observed in the vicinity of the crater and flank wear, locations at which Ti-64 has adhered. Although in the bulk the features are also noticeable, therefore the cavities are most likely not a phenomenon that occurred during machining. Since the darker regions are found throughout the insert and not only near the cutting edge.

5.2.2 M1

The worn M1 milling insert has cracks advancing from the cutting edge, these are probably generated during machining or at the polishing stage during sample preparation. In the Co binder no voids are present, but it is not certain that cavities are absent during machining since the cutting edge has most likely fractured in the latter stage of machining. This is because the insert has lost the original insert geometry and an adverse cutting edge geometry increases the risk of fracture.

5.2.3 M2

The worn M2 milling insert has no pore-like features in the insert except in the red square region presented in figure 31. The darker patches in the binder phase are conceivable voids, it is difficult to state that the features are pores. Since the SE-SEM image showed a more defined contrast of the voids while the BSE-SEM images are more diffuse, the surface sensitive SE-SEM image indicates that they are indeed voids. Near the voids Ti-64 has adhered to the cutting edge, both under and above the red region of interest no voids are seen and neither adhered Ti-64. This is interesting, why are there only voids where Ti-64 has adhered? A possible explanation is that regions where no voids are observed has recently fractured away. This theory is supported by the fact that the red square region is the least worn, it is closest to the unworn outline boundary.

The reason for the voids is difficult to state, it can only be noted that they are found 15 µm from the cutting edge and are <0.5 µm. The cause might be Kirkendall porosity where Co diffuses outwards to the Ti-64 at a faster rate than the Ti diffusing into the binder phase. It is difficult to validate that this is the reason but the voids are found along the WC/Co interface. The nucleation of Kirkendall voids is usually found at dislocations or grain boundaries due to a lower nucleation energy, in this case the WC/Co interface. The rounded shape and dispersion of the voids is also an indication of Kirkendall porosity.

The second theory to the origin of the voids might be because of the fast outwards diffusion of C into Ti-64, simultaneously the W from the WC grains dissolve in the Co binder as shown in figure 36. The C diffuses at a faster rate than both Co and W, this because of the driving force to form TiC due to a lower energy state compared to WC [26]. The outwards diffusion of C leads to a volume change inside the cemented carbide.

As an example, assuming an initial 1 cm^3 cemented carbide volume of which 0.785 cm^3 is WC and 0.215 cm^3 Co, corresponding to the composition of sample M2. Suppose that the volume of dissolved WC is proportionate to a 7% W concentration in the Co, the C dissolves into the Ti-64 and is disregarded since it is removed during machining. The initial cobalt is 0.215 cm^3/6.69 $cm^3 mole^{-1}$ = 0.0315 mole, the molar volume of pure Co at room temperature is used [59]. Assuming a 7 % concentration of W in the Co binder, it would imply $n_W/(n_W+0.0315)=0.07$ where n_W is the molar amount of dissolved W in the Co and also disintegrated WC n_{WC}. The solution to the equation is $n_W=0.0024$ mole. The volume decreased is 0.0024

mole*12.5 $cm^3 mole^{-1}$ = 0.0024 cm^3, the molar volume of WC at room temperature is used [59]. Similarly the volume increase of the cobalt binder is calculated by multiplying the amount of Co with the molar volume difference between pure Co and Co with 7% W, (6.83-6.69)$cm^3 mole^{-1}$ * n_{Co} mole=0.0044 cm^3. The resulting volume change (1+increased volume in the Co - decreased volume in the WC)/1 = 0.975, a corresponding 2.5 % volume change reduction.

The decrease in volume might exhibit as pore formation in the cemented carbide as seen in figure 36. Many assumptions were made in this example but it shows that the volume change of outwards C diffusion leads to a volume change. Although 2.5% decrease in volume does not entirely match the cavity proportion of ~ 0.43% found in the M2 sample, the second hypothesis should be considered as a possibility.

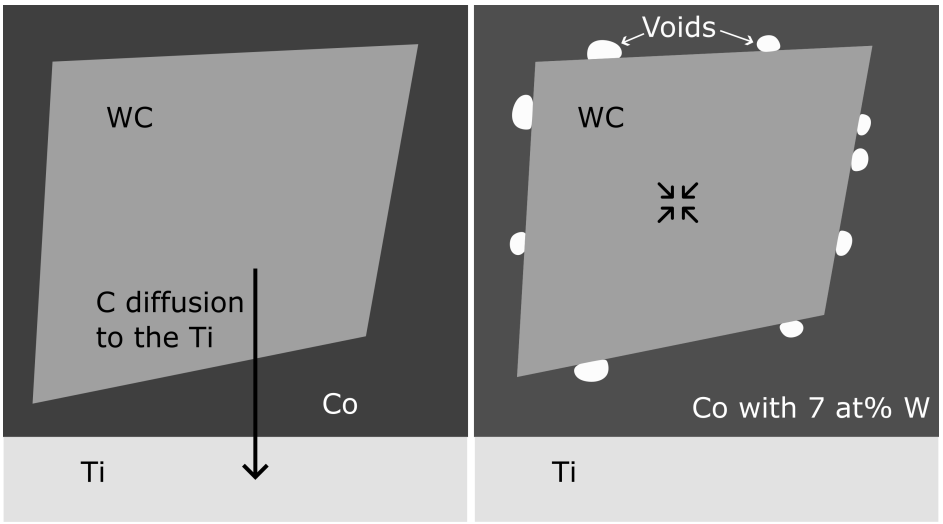

Figure 36: Schematic illustration of the volume change in the cemented carbide when C diffuses to the Ti and the matching W is dissolved in the Co binder.

5.2.4 M3

The worn M3 milling insert sample has residual debris on the Bakelite which is believed to be excess from the clamps used during Bakelite mounting in the sample preparation step. Since no XEDS data was collected it is not confirmed. Assuming that it is residual debris, no adhered Ti-64 is observed on the cutting edge. The insert is worn and the geometry is unfavorable which indicates that the sample most likely has fractured during the latter stage of machining. The groups of cavities in the binder phase which are observed at several locations has a particular appearance, they fill the previous binder phase volume in between the WC grains. The cavities are of irregular shape, sparse and infrequently found, therefore the cavities are reasonably not Kirkendall porosity. A possible explanation would be that the intergranular cavities are formed during plastic deformation. This is supported by the irregular shape and the disadvantageous cutting geometry which creates higher cutting temperatures increasing the risk of plastic deformation as stated in section 2.4.2.

5.3 Future work

The static diffusion couple experiment does not represent the machining conditions completely. New layer phases such as η-phase, (Ti,V)C and bcc W are found, in which the diffusion of Co and Ti is unknown. However, further diffusion couple experiments can answer why voids are found in some diffusion couples and not in others. In the 1200 °C Ti-64/H13A 2.5 GPa and 1000 °C Ti-5553/H13A 35 MPa samples cavities are observed. These samples have a high ramp rate during annealing and therefore it is believed that the possible Kirkendall pores are formed before the diffusion barriers are created. A future experiment with a

high ramp rate >100 °C/min but with a different diffusion couple method as for the 35 MPa and 2.5 GPa samples would give further insight into why cavities are found only in certain diffusion couples.

The study aims to investigate the Kirkendall porosity in Ti machining, where Co diffuses at a faster rate than the Ti. Therefore a Ti/Co diffusion couple would be favorable, however, since additional phases form in the diffusion couple it would give little insight [47]. This because new phases Co_3Ti, Co_2Ti, CoTi and $CoTi_2$ are not present during titanium machining.

In this study the worn inserts were all immensely worn and has lost their cutting geometry. Additional studies investigating insert with minor fracture and chip wear and an intact cutting geometry is of interest. Are the cavities found in the worn M2 insert present before fracture and are the voids a leading cause for fracture and chipping wear.

Future research could apply computational diffusion simulations and combine it with experimental observations. By simulating the diffusion process and assuming that the diffusion mechanism is substitutional the Kirkendall pore formation can be predicted [60].

6 Conclusion

The project has resulted in the following conclusions.

- The possibility of Kirkendall porosity during titanium machining is indecisive. It is supported by the high diffusion of Co in Ti and lower diffusion of Ti in Co, more than 3 orders of magnitude difference.
- Diffusion couple samples with a high ramp rate during annealing have voids <1 μm in the η-phase. The pores are found in the 1200 °C Ti-64/cemented carbide 2.5 GPa and 1000 °C Ti-5553/H13A 35 MPa samples.
- Diffusion couple samples with a low ramp rate during annealing has no voids in the η-phase. These samples are 1200, 1000 °C Ti-5553/H13A and Ti-64/H13A 850 MPa diffusion couples. The absence of pores in the η-phase agrees with previous diffusion couple studies with low ramp rates [30][55]. The intermediate phases (Ti,V)C, W and η-phase hinder the diffusion and act as barriers. Since the diffusion barriers are thicker in the samples with low ramp rates, it is believed that the thickness of the barriers impede the pore formation.
- The high pressure during annealing in the 1200 °C Ti-64/cemented carbide 2.5 GPa sample is not enough to suppress the pore formation.
- The diffusion couple procedure applied in the ~ 0 pressure samples does not produce a diffusion couple with a comprehensible and strong diffusion bond. The technique includes Ti sandwiched in between a sectioned insert, no clamping or pressure is applied during the annealing.
- Small voids are found in the Co binder in a worn turning insert. They are probably not formed during machining since the voids are present not only along the cutting edge but also in the bulk.
- The cross section of 5 worn milling inserts were investigated, in three of the inserts no pores were found. In one insert (M2) pores were observed at the cutting edge and 15 μm inwards, these are suggested to be formed during machining due to diffusion wear. In another insert (M3) intergranular cavities are present, these are proposed to be formed by plastic deformation during machining.

References

[1] *Titanium Matrix Composites*, pages 4–46. Springer Berlin Heidelberg, Berlin, Heidelberg, 2007.

[2] James D Cotton, Robert D Briggs, Rodney R Boyer, Sesh Tamirisakandala, Patrick Russo, Nikolay Shchetnikov, and John C Fanning. State of the art in beta titanium alloys for airframe applications. *Jom*, 67(6):1281–1303, 2015.

[3] G.S Upadhyaya. Materials science of cemented carbides — an overview. *Materials Design*, 22(6):483–489, 2001. 1.Selected Papers from the 3rd International Conference on Cast Metal Matrix Composites 2. Advances in Cemented Carbides.

[4] Mehdi Hourmand, Mohammad S. Uddin, and Ahmed A.D. Sarhan. Processing of titanium by machining: A closer look into performance metrics in bio-fabrications. In *Reference Module in Materials Science and Materials Engineering*. Elsevier, 2017.

[5] Alex Graves, Armin Salmasi, Simon J Graham, Wei Wan, Changhong Xiao, Martin Jackson, Henrik Larsson, and Susanne Norgren. An experimental and theoretical investigation on ti-5553/wc–co (6%) chemical interactions during machining and in diffusion couples. *Wear*, 516:204604, 2023.

[6] C. Leyens and M. Peters. *Titanium and Titanium Alloys*. John Wiley Sons, Ltd, 2003.

[7] Alokesh Pramanik and Guy Littlefair. Machining of titanium alloy (ti-6al-4v)—theory to application. *Machining Science and Technology*, 19(1):1–49, 2015.

[8] T.R. Bieler, R.M. Trevino, and L. Zeng. Alloys: Titanium. In Franco Bassani, Gerald L. Liedl, and Peter Wyder, editors, *Encyclopedia of Condensed Matter Physics*, pages 65–76. Elsevier, Oxford, 2005.

[9] G Fantozzi M Gordon, S Etienne. *Euro-ceramics*. vol 3, Elsevier Applied Sc, New York, 1989.

[10] P U; Gustafson D A (editors) L Ho-Yi, Y Jinghui; Gummeson. Modern developments in powder metallurgy; proceedings of the international powder metallurgy conference, orlando, fl, june 5-10, 1988. volumes 18, 19, 20, and 21.

[11] David A Stephenson and John S Agapiou. *Metal cutting theory and practice*. CRC press, 2018.

[12] Sandvik Coromant AB. Machining formulas and definitions. 2023.

[13] Edward M. Trent Paul K. Wright. *Metal Cutting*. Butterworth–Heinemann, 2000.

[14] Mikael Fallqvist. Microstructural, mechanical and tribological characterisation of cvd and pvd coatings for metal cutting applications. pages 13–24, 01 2012.

[15] Stina Odelros. Tool wear in titanium machining. *M.Sc. Thesis, Uppsala university*, 2012.

[16] Toshiyuki Obikawa Yasuo Yamane Thomas Childs, Katsuhiro Maekawa. *Metal Machining Theory and Applications*. Arnold,a member of the Hodder Headline Group, 2000.

[17] PK Wright and A Bagchi. Wear mechanisms that dominate tool-life in machining. *Journal of Applied Metalworking*, 1:15–23, 1981.

[18] Lisa Toller and Susanne Norgren. Mechanisms of plastic deformation in wc-co and wc-ni-fe turning inserts. In *Proceedings of the 19th Plansee Seminar. Austria: Plansee Group*, 2017.

[19] Gustaf Östberg, Katharina Buss, Mikael Christensen, Susanne Norgren, Hans-Olof Andrén, Daniele Mari, Göran Wahnström, and Ingrid Reineck. Effect of tac on plastic deformation of wc–co and ti(c,n)–wc–co. *International Journal of Refractory Metals and Hard Materials*, 24(1):145–154, 2006. Science of hard materials-8. Part II. Selected papers from the 8th International Conference on the Science of Hard Materials.

[20] M.A. Yousfi, J. Weidow, A. Nordgren, L.K.L. Falk, and H.-O. Andrén. Deformation mechanisms in a wc–co based cemented carbide during creep. *International Journal of Refractory Metals and Hard Materials*, 49:81–87, 2015. Special Issue: International Conference on the Science of Hard Materials – 10.

[21] M Ibrahim Sadik, Martina Lattemann, and José García. Specific carbide substrate design to enhance tool performance in machining of ti5553. *Procedia CIRP*, 77:598–601, 2018.

[22] Y Su, N He, Li Li, and XL Li. An experimental investigation of effects of cooling/lubrication conditions on tool wear in high-speed end milling of ti-6al-4v. *Wear*, 261(7-8):760–766, 2006.

[23] Mohammed Nouari and Hamid Makich. Experimental investigation on the effect of the material microstructure on tool wear when machining hard titanium alloys: Ti–6al–4v and ti-555. *International Journal of Refractory Metals and Hard Materials*, 41:259–269, 2013.

[24] A Jawaid, Safian Sharif, and S Koksal. Evaluation of wear mechanisms of coated carbide tools when face milling titanium alloy. *Journal of materials processing technology*, 99(1-3):266–274, 2000.

[25] S. Odelros, B. Kaplan, M. Kritikos, M. Johansson, and S. Norgren. Experimental and theoretical study of the microscopic crater wear mechanism in titanium machining. *Wear*, 376-377:115–124, 2017. 21st International Conference on Wear of Materials.

[26] Paul Dudley Hartung, BM Kramer, and BF Von Turkovich. Tool wear in titanium machining. *CIRP Annals*, 31(1):75–80, 1982.

[27] Wang Min, Wang Min, and Zhang Youzhen. Diffusion wear in milling titanium alloys. *Materials science and technology*, 4(6):548–553, 1988.

[28] CB Pollock and HH Stadelmaier. The eta carbides in the fe- w- c and co- w- c systems. *Metallurgical Transactions*, 1:767–770, 1970.

[29] CM Moreno, G Artola, and JM Sanchez. Interaction between ti-6% al-4% v alloys and hardmetals coated by cathodic-arc technology. In *Materials Science Forum*, volume 492, pages 353–358. Trans Tech Publ, 2005.

[30] R M'Saoubi, M Schwind, B Kaplan, and B Jansson. Chemical interactions between cemented carbide and difficult-to-machine materials by diffusion couple method and simulations. *Journal of Phase Equilibria and Diffusion*, 39:369–376, 2018.

[31] LB Pfeil et al. The oxidation of iron and steel at high temperatures. *Journal of Iron and Steel Inst*, 119:501–547, 1929.

[32] EO Kirkendall and AD Smigelskas. Zinc diffusion in alpha brass. *Aime Trans*, 171:130–142, 1947.

[33] Aloke Paul, Tomi Laurila, Vesa Vuorinen, and Sergiy V. Divinski. *Interdiffusion and the Kirkendall Effect in Binary Systems*, pages 239–298. Springer International Publishing, Cham, 2014.

[34] GS Hartley and JF Crank. Some fundamental definitions and concepts in diffusion processes. *Transactions of the Faraday Society*, 45:801–818, 1949.

[35] A Paul, M.J.H van Dal, A.A Kodentsov, and F.J.J van Loo. The kirkendall effect in multiphase diffusion. *Acta Materialia*, 52(3):623–630, 2004.

[36] Ven Young Doo and RW Balluffi. Structural changes in single crystal copper-alpha brass diffusion couples. *Acta metallurgica*, 6(6):428–438, 1958.

[37] Aloke Paul. The kirkendall effect in solid state diffusion. *Automation in Construction - AUTOM CONSTR*, 01 2004.

[38] S. Prasad and A. Paul. Growth mechanism of phases by interdiffusion and diffusion of species in the niobium–silicon system. *Acta Materialia*, 59(4):1577–1585, 2011.

[39] Gary M Gladysz and Krishan K Chawla. *Voids in materials: from unavoidable defects to designed cellular materials*. Elsevier, 2020.

[40] E. Santos and F. Dyment. Solvent and solute diffusion in b.c.c. ti-co and ti-mn alloys. *Philosophical Magazine*, 31(4):809 – 827, 1975.

[41] Hideo Nakajima, Masahiro Koiwa, Yasuhide Minonishi, and Sakai Ono. Diffusion of cobalt in single crystal alpha;-titanium. *Transactions of the Japan Institute of Metals*, 24(10):655–660, 1983.

[42] C. M. Dyment, F. Libanati. Self-diffusion of ti, zr, and hf in their hcp phases, and diffusion of nb95 in hcp zr. *Journal of Materials Science*, 3:349–359, 1968.

[43] E. Santos and Fanny Dyment. Solvent and solute diffusion in b.c.c. ti—co and ti—mn alloys. *Philosophical Magazine*, 31:809–827, 1975.

[44] RF Peart and DH Tomlin. Diffusion of solute elements in beta-titanium. *Acta metallurgica*, 10(2):123–134, 1962.

[45] Milton Ohring. *Interdiffusion, Reactions, and Transformations in Thin Films*, pages 641–710. 12 2002.

[46] S Neumeier, HU Rehman, J Neuner, CH Zenk, S Michel, S Schuwalow, J Rogal, R Drautz, and M Göken. Diffusion of solutes in fcc cobalt investigated by diffusion couples and first principles kinetic monte carlo. *Acta Materialia*, 106:304–312, 2016.

[47] Peter JM van der Straten, Guillaume F Bastin, Frans JJ van Loo, and Gerard D Rieck. Phase equilibria and interdiffusion in the cobalt-titanium system. *Z. Metallkd*, 67:152–157, 1976.

[48] R.S Barnes and D.J Mazey. The effect of pressure upon void formation in diffusion couples. *Acta Metallurgica*, 6(1):1–7, 1958.

[49] J. Klein, G. Warshaw, N. Dudziak, S. Cogan, and R. Rose. On the suppression of kirkendall porosity in multifilamentary superconducting composites. *IEEE Transactions on Magnetics*, 17(1):380–382, 1981.

[50] Elman C Jameson. *Electrical discharge machining*. Society of Manufacturing Engineers, 2001.

[51] Ahmet Hasçalık and Ulaş Çaydaş. A comparative study of surface integrity of ti–6al–4v alloy machined by edm and aecg. *Journal of Materials Processing Technology*, 190(1):173–180, 2007.

[52] Natasha Erdman, David C. Bell, and Rudolf Reichelt. *Scanning Electron Microscopy*, pages 229–318. Springer International Publishing, Cham, 2019.

[53] Rebecka Lindvall, Axel Bjerke, Armin Salmasi, Filip Lenrick, Rachid M'Saoubi, Jan-Eric Ståhl, and Volodymyr Bushlya. Predicting wear mechanisms of ultra-hard tooling in machining ti6al4v by diffusion couples and simulation. *Journal of the European Ceramic Society*, 43(2):291–303, 2023.

[54] Rebecka Lindvall, Filip Lenrick, Rachid M'Saoubi, Jan-Eric Ståhl, and Volodymyr Bushlya. Performance and wear mechanisms of uncoated cemented carbide cutting tools in ti6al4v machining. *Wear*, 477:203824, 2021. 23rd International Conference on Wear of Materials.

[55] Finn Giuliani Pete Crawforth Bradley Wynne Oliver Hatt, Henrik Larsson and Martin Jackson. Predicting chemical wear in machining titanium alloys via a novel low cost diffusion couple method. *Procedia CIRP*, 45:219–222, 2016. 3rd CIRP Conference on Surface Integrity.

[56] Anita Iannucci, A. A. Johnson, Edward J. Hughes, and P. W. Barton. Study of the solubility limits of the compound tico using high-temperature x-ray diffractometry. *Journal of Applied Physics*, 39:2222–2224, 1968.

[57] S Sarian. Diffusion of 44ti in tic x. *Journal of Applied Physics*, 40(9):3515–3520, 1969.

[58] Deepak G Bhat, Vikram A Bedekar, and Stephen A Batzer. A preliminary study of chemical solubility of ultra-hard ceramic almgb14 in titanium: Reconciliation of model with experiment. *Machining science and technology*, 8(3):341–355, 2004.

[59] Björn Uhrenius. Evaluation of molar volumes in the co w c system and calculation of volume fractions of phases in cemented carbides. *International Journal of Refractory Metals and Hard Materials*, 12(3):121–127, 1993.

[60] Henrik Strandlund and Henrik Larsson. Prediction of kirkendall shift and porosity in binary and ternary diffusion couples. *Acta Materialia*, 52(15):4695–4703, 2004.

[61] Z. Nibennaoune, Daniel George, Said Ahzi, David Ruch, Yves Rémond, and J.J. Gracio. Numerical simulation of residual stresses in diamond coating on ti-6al-4v substrate. *Thin Solid Films*, 518:3260–3266, 04 2010.

[62] E. Trofimov, R. Lutfullin, and Rishat Kashaev. Elastic properties of the titanium alloy ti-6al-4v. *Letters on Materials*, 5:67–69, 01 2015.

7 Appendix

A Thermal expansion

When changing the temperature of a body the dimensions will change correspondingly. The change in length δl is dependent on the thermal expansion coefficient α, the initial length l_0 and the temperature change. Using equation 1 the expansion or contraction can be calculated, an assumption that the equation is linear simplifies the equation.

$$\delta l = \alpha l_0 \delta T \qquad \Delta l = \alpha l_0 \Delta T \tag{1}$$

When a body during thermal expansion is restricted it will undergo thermal strain ϵ_{th}, with strain the piece experience stress σ_{th}. The relation between the stress and strain is linear proportional until the yield strength of the material, the relation is related to the modulus of elasticity E, see equation 2.

$$\sigma_{th} = E\epsilon_{th} = E\frac{\Delta l}{l} \tag{2}$$

During the diffusion couple both the titanium and the tungsten carbide insert will expand, see figure A.1. The thermal expansion coefficient for titanium is higher compared to tungsten carbide which leads to restrictions in the titanium expansion. With an initial radius of 2.578 mm the radius expansion Δr is calculated using equation 1 with a temperature difference $\Delta T = 980°C$, see table 5. Since tungsten carbide has a higher modulus of elasticity compared to titanium alloy the final tungsten carbide/titanium interface is assumed to be restricted by the expansion of the tungsten carbide. The titanium will therefore be compressed, the thermal stress is calculated using equation 2 were $\Delta l = \Delta r_{Ti64} - \Delta r_{CC}$ and the elasticity of Ti-64 is used. The thermal stress is only determined for Ti-64 at 1000 °C, the thermal stress during annealing is calculated to ~850 MPa.

Table 5: The thermal expansion coefficient, modulus of elasticity and radius expansion for cemented carbide and Ti-64 at 1000 °C [3][61][62].

Element	Thermal expansion coefficient α [μK^{-1}]	Modulus of elasticity E [GPa]	r [mm]
Tungsten carbide (6 wt% Co)	4.7-5	630	2.591
Ti-64	13	~ 110	2.611

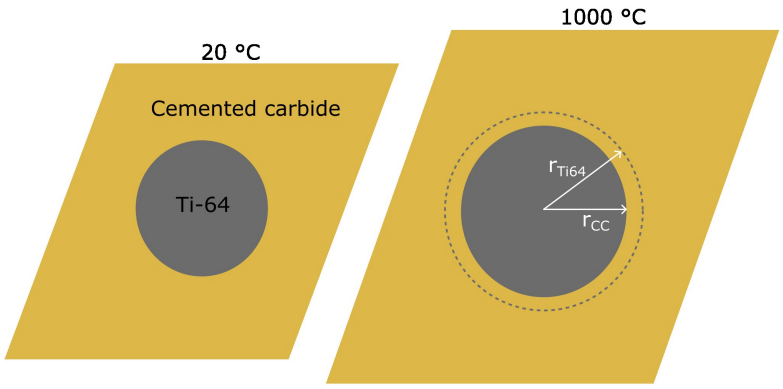

Figure A.1: Schematic illustration of the thermal expansion during annealing, the expansion radius of both Ti-64 and cemented carbide is indicated.